Int J Earth Sci (Geol Rundsch) (2017) 106:1753–1772
DOI 10.1007/s00531-016-1384-2

ORIGINAL PAPER

Depositional environment and origin of the Lilaozhuang Neoarchean BIF-hosted iron–magnesite deposit on the southern margin of the North China Craton

Hua Huang[1] · LianChang Zhang[1] · Sébastien Fabre[2] · ChangLe Wang[1] · MingGuo Zhai[1]

Received: 3 December 2015 / Accepted: 2 August 2016 / Published online: 13 August 2016

Abstract The Neoarchean Lilaozhuang iron–magnesite deposit is located in the middle of the Huoqiu banded iron formation (BIF) ore belt in Anhui Province on the southern margin of the North China Craton. The Huoqiu BIF is the unique one that simultaneously develops quartz-type, silicate-type, and carbonate-type magnetite in the region. The Lilaozhuang deposit is characterized by magnesium-rich carbonate (magnesite) in magnetite ores. The BIF-hosted iron ores include mainly of silicate type and carbonate type, with a small amount of quartz type, which chiefly exhibit banded and massive structure, with minor disseminated structure. The magnesite ores occur as crystal-like bright white and exhibits massive structure. The Y/Ho ratio and REY pattern of both iron and magnesite ores are similar to that of seawater, while Eu shows positive anomaly, which is the sign of seafloor hydrothermal mixture. These features suggest that ore-forming materials of iron and magnesium in the Lilaozhuang deposit are mainly from the mixture of seafloor hydrothermal and seawater. Both ores do not exhibit negative Ce anomaly, which indicates that the deposit was formed in an environment showing a lack of oxygen. C–O isotopic compositions indicate that magnesite ore has been reformed by metamorphism of low amphibolite facies and later hydrothermal alteration. Based on the comprehensive analysis, authors suggest that iron and magnesite ores in the Lilaozhuang deposits formed in a confined sea basin on continental margin and was influenced by later complex geological processes.

Keywords The Lilaozhuang BIF · Magnesite · C–O isotopes · Material sources · Depositional environment · Ore-forming process

✉ LianChang Zhang
lczhang@mail.igcas.ac.cn

[1] Key Laboratory of Mineral Resources, Institute of Geology and Geophysics, Chinese Academy of Sciences, No. 19, Beitucheng Western Road, Chaoyang District, Beijing 100029, People's Republic of China

[2] IRAP-OMP, CNRS-University of Toulouse, 31400 Toulouse, France

Introduction

Precambrian banded iron formation (BIF) is iron-rich minerals (mainly magnetite) and gangue minerals (mainly quartz) consisting of banded or striped formation chemical sedimentary rocks (James 1954, 1983), widely distributed around the world in Archean to Early Proterozoic (3.8–1.9 Ga) (Huston and Logan 2004), and develops well around 2.7–2.0 Ga (Isley 1995; James 1983; Klein 2005). It is an important part of the early crust, recorded much information about the evolution of lithosphere, hydrosphere, atmosphere, and biosphere of the earth, reflecting geological environment and crustal evolution characteristics at that time. According to the age and ore-bearing formation, the BIF is classified as Algoma type and Superior type (Gross 1980). Algoma type is mainly produced in Archean, usually formed in island arc, back-arc basin or cratonic rift, and closely related with submarine volcanic activity. Superior type is mainly produced in Early Proterozoic, generally formed in shallow marine environment and closely related to sedimentation, with the deposition scale much larger than Algoma type (Gross 1980, 1983, 1996). Chinese geologists have been studying BIFs systematically since the 1950s (Cheng 1957). It was shown that the Chinese BIFs mainly developed in the edge and rift zones of the North China Craton (NCC) from the Late Archean to Early Proterozoic, with the primary characteristics of low-grade ore

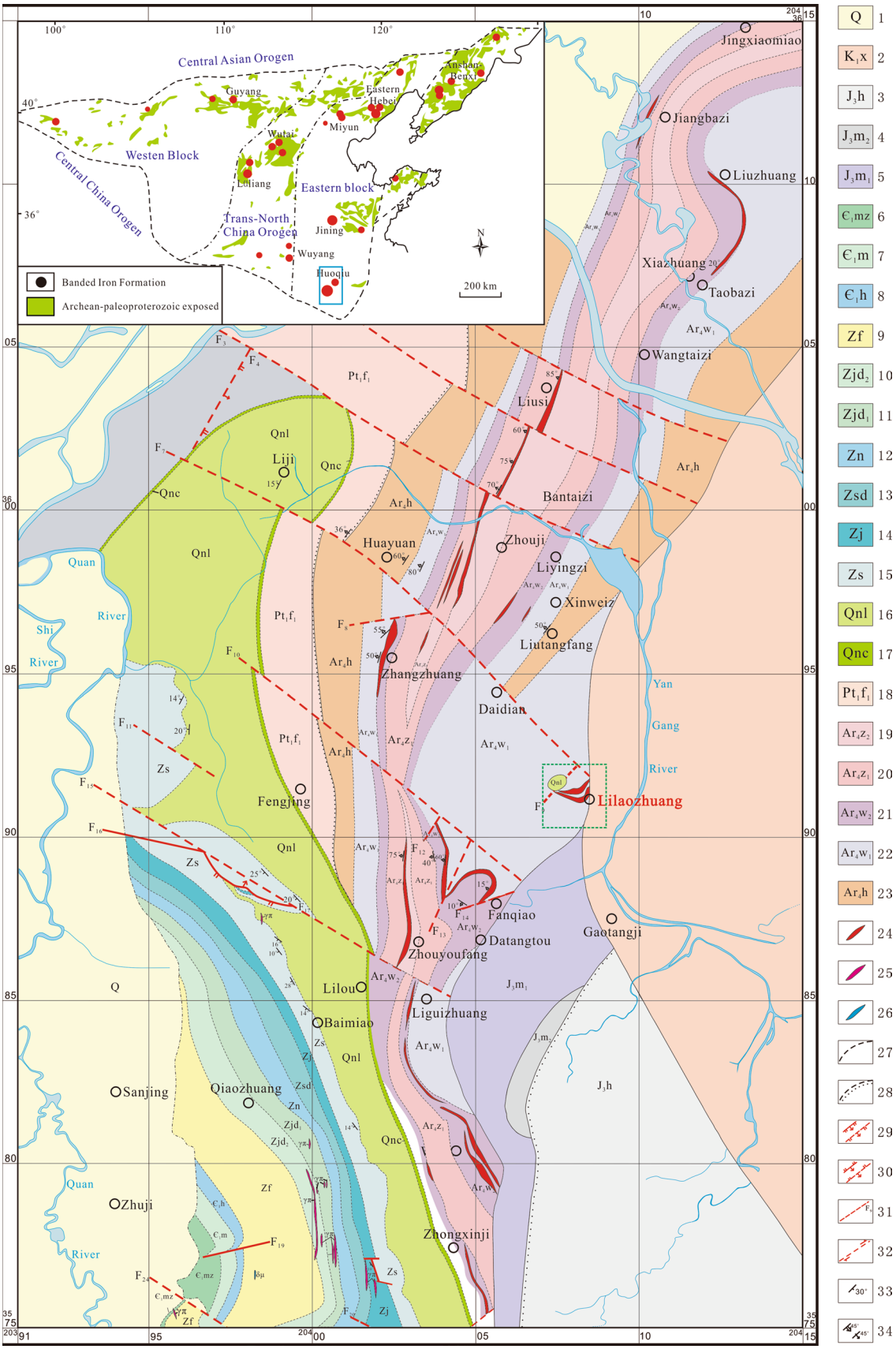
Central Asian Orogen
Central China Orogen
Trans-North China Orogen
Westen Block
Eastern block
Guyang
Wutai
Miyun
Eastern Hebei
Xinshan-Benxi
Lvliang
Jining
Wuyang
Huoqiu
Banded Iron Formation
Archean-paleoproterozoic exposed
200 km
Jingxiaomiao
Jiangbazi
Liuzhuang
Xiazhuang
Taobazi
Wangtaizi
Liusi
Bantaizi
Zhouji
Liyingzi
Xinweiz
Liutangfang
Huayuan
Zhangzhuang
Daidian
Lilaozhuang
Fanqiao
Datangtou
Zhouyoufang
Gaotangji
Liguizhuang
Lilou
Baimiao
Fengjing
Liji
Sanjing
Qiaozhuang
Zhuji
Zhongxinji
Quan River
Shi River
Yan Gang River
Q
Qnl
Qnc
Zs
Zj
Zf
Zsd
Zn
Ar4h
Pt1f1
Ar4w1
Ar4w2
Ar4z1
Ar4z2
J3h
J3m1
J3m2

◂**Fig. 1** Geological map of the Huoqiu ore deposit (313 Geological Team 1991; Zhao et al. 2005). *1* Quaternary; *2* lower Cretaceous Xinzhuang formation; *3* upper Jurassic Heishidu formation; *4* upper Jurassic upper section of Maotan formation; *5* upper Jurassic lower section Maotan formation; *6* lower Cambrian Maozhuang formation; *7* lower Cambrian system Mantou formation; *8* lower Cambrian system Houjiashan formation; *9* Sinian system Fengtai formation; *10* Sinian system upper section of Jiudingshan formation; *11* Sinian system lower section of Jiudingshan formation; *12* Sinian system Niyuan formation; *13* Sinian system Sidingshan formation; *14* Sinian system Jiuliqiao formation; *15* Sinian system Sishilichangshan formation; *16* Neoproterozoic (Qingbaikou system) Liulaobei formation; *17* Neoproterozoic (Qingbaikou System) Caodian formation; *18* Paleo-Proterozoic Xiayan formation, Fengyang Group; *19* Neoarchean upper section of Zhouji formation, Huoqiu Group; *20* Neoarchean lower section of Zhouji formation, Huoqiu Group; *21* Neoarchean upper section of Wuji formation, Huoqiu Group; *22* Neoarchean lower section of Wuji formation, Huoqiu Group; *23* Neoarchean Huayuan formation, Huoqiu Group; *24* ore body; *25* granite porphyry; *26* diorite porphyrite; *27* measured-speculated geological boundaries; *28* speculated unconformity geological boundaries; *29* speculated normal faults; *30* speculated thrust fault; *31* indeterminacy fault and its serial number; *32* speculated fault; *33* attitude of stratum; *34* schistosity and inverted schistosity occurrence

and less rich ore. They almost all belong to Algoma-type deposits, such as Gongchangling, Waitoushan, Nanfen, and Qidashan iron deposit in Liaoning Province, and Shuichang, Shirengou, and Sijiaying iron deposit in the east of Hebei Province. Only Yuanjiacun iron ore in Shanxi Province is initially thought as Superior type (Zhai and Windley 1990; Zhai et al. 1990; Cheng 1998; Dai et al. 2012, 2014; Wang et al. 2014; Zhang et al. 2011, 2012; Shen et al. 1994, 2006). In recent years, some researchers suggest that the Huoqiu BIF is a sedimentary metamorphic ore deposit formed in back-arc basin with age of 2.75–2.55 Ga, and the origin for mineralization is mainly from seawater, submarine volcanic hydrothermal, and a small amount of terrigenous clastic materials (Liu and Yang 2015; Wan et al. 2009; Yang et al. 2012, 2014). Based on the formation environment, flysch-like structure of ore-bearing reservoirs and abundant occurrence of carbonate rocks in the Huoqiu iron area (Yang et al. 2012), Liu and Yang (2015) define it as the Superior-type BIF.

Most of the BIFs in NCC can be divided into quartz-type (the oxide type) magnetite (or hematite) and silicate-type magnetite (or hematite) according to the features of mineral assemblage. However, the Lilaozhuang BIF in the Huoqiu area contains not only these two types but also carbonate type. Besides, the Lilaozhuang iron deposit also occurs with magnesite deposit, which is also very rare compared with other BIFs in the world. By analyzing the major, trace elements of iron ore, magnesite and bedrock of the Lilaozhuang deposit at the Huoqiu area, as well as C–O isotopics of magnesites and carbonate mineral associated with magnetites, this paper discusses the formation tectonic setting, sedimentary environment, and origin of the Lilaozhuang deposit.

Regional geology

The Precambrian Huoqiu BIF iron orefield is located in the southern margin of NCC. There are Zhouji, Zhangzhuang, Zhouyoufang, Wuji, Zhongxinji, Lilaozhuang, and other iron deposits from north to south (Fig. 1), The Huoqiu orefield is composed of more than 10 iron deposits with total proven reserves of ca. 23×10^8 t (contained Fe metal), and probable reserves of ca. 30×10^8 t, with average w (Fe) = 23.74 % (313 Geological Team 1995). Huoqiu iron orefield is located at the Changshanqiong fault-fold belt and situated in western Huoqiu County with north–south extension about 40 km and west–east width about 2.7 km. The east of Huoqiu orefield is Hefei depression (secondary structure—Huoqiu depression), and the west is Huangchuan depression in Henan Province (secondary structure—Gushi depressions), with Feizhong major fault as south boundary and Huainan synclinorium as northern neighbor.

The Precambrian metamorphic basement of Huoqiu iron orefield is part of Henan and Anhui partitions of North China tectonic zone and is composed of Neoarchean Huoqiu Group, Wuhe Group, and Early Proterozoic Fengyang Group. The regional stratigraphy develops Neoarchean—Quaternary strata except for some missing Paleozoic strata. The Huoqiu iron orefield is mainly hosted in the Neoarchean Huoqiu Group, which is a set of metamorphic rocks which experienced Archean middle-high-grade metamorphism. According to the rock associations, the Huoqiu Group can be divided into two series and three succession formations, i.e., the Huayuan Fm., Wuji Fm., and Zhouji Fm. These three formations are all in conformable contacts. The total thickness of Huoqiu Group and iron-bearing layer in Huoqiu area is >1520 m, and they have all been covered by Quaternary sediments. The Huoqiu Group is characterized by both sedimentary and volcanic sedimentary formations. The protolith of Huoqiu Group is considered to be flysch-like nature formed by a basic volcanic–sedimentary cycle, that is, terrestrial clastic rocks–clay shale–carbonate rocks interbedded with ferrosilicon sedimentary formation. Yang et al. (2012) have presumed Huoqiu Group to be the sedimentary products deposited between island arc and continental margin. The BIF occurs in a north–south-trending trough in an east–west depression.

From the regional geological background, the Huoqiu Group consists of metamorphic volcanic–sedimentary rocks which have undergone migmatization. The mineral assemblage of hornblende + almandine + plagioclase + quartz

Table 1 Ore types and their features at Huoqiu deposits

Ore type	Mineral assemblage	Texture and structure	Occurrence locations
Silicate	Hornblende–quartz–magnetite	Banded, striped structure and columnar, granular texture	Most parts of Huoqiu deposit
	Iron amphibole–quartz–magnetite		
	Actinolite–quartz–magnetite		
Quartz	Quartz–magnetite	Banded, striped structure and fine crystalloblastic texture	Zhouji, Zhouyoufang, and Zhongxinji deposits
	Quartz–hematite/specularite	Banded, striped structure and flake crystalloblastic texture	
Carbonate	Magnetite–magnesite	Fine crystalloblastic texture	Only at Lilaozhuang deposit
	Magnetite–iron magnesite		

may indicate low amphibolite facies of regional metamorphism during metallogenic stages in the Huoqiu orefield. In addition, local disseminated-type ore formation and the emergence of serpentine (e.g., Lilaozhuang deposit) shows that metallogenic stage had undergone hydrothermal metasomatism (Sun 2007), similar to those as reported for hydrothermal reformation in NCC. A small amount of carbonate magnetites occurs at Lilaozhuang area, which is accompanied by the emergence of a large amount of magnesite. Lilaozhuang deposit is the representative of Huoqiu BIF mineralization belt, with bedrocks that occur in iron ore body contain large amounts of carbonate rocks and produce associated thick layered magnesite, which is featured by paragenetic association of iron–(iron) magnesite (Table 1).

Deposit geology

The Lilaozhuang iron–magnesite ore deposit in the eastern Huoqiu orefield was controlled by a syncline tectonic trending east–west direction, with proven reserves of iron ore resources ca. 64×10^6 t and magnesite reserves ca. 33×10^5 t (Department of Land and Resources of Anhui Province 2004). The iron–magnesite ore bodies are hosted in meta-sedimentary rocks and marbles of the Wuji formation in the Neoarchean Huoqiu Group. The lithology of the Lilaozhuang syncline core is the bottom section of Late Archean Zhouji formation, composed of banded migmatite and migmatized mica-plagiogneiss. Both limbs of the syncline are Wuji formation, but the dip angles of the limbs look different, with the south limb (20°–40°) is a little steeper than the north limp (about 20°),the axial plane is smooth and leans to the south slightly. The upper part of the top section of Wuji formation contains magnetite-bearing schist, migmatite layer, gneiss layer, and the lower part bears magnetite mixed with magnesium-rich carbonate layer and gneiss layer. The bottom section is mainly homogeneous migmatite, with lithology chiefly biotite plagiogneiss, mica–quartz schist, magnetite sandwiched magnesite, magnesite, serpentinite, and actinolite schist (Sun 2007).

Ore body

The ore body is covered by Quaternary clay of 136–243 m thick, with length of 1187 m from east to west, and width of 286–1028 m from south to north (Fig. 2). The ore body is generally layered, stratiform-like, or lenticular, showing an overall trend of nearly east–westward with asymmetrical wings. Along the strike and dip, the ore body displays diverse features, e.g., dilatation, striction, offset, recombination, and pinching out (Figs. 2, 3a). Two faults have been found in the mining area. F14 is about 1000 m, located in the eastern part of ore deposit showing a normal fault with the strike NW 317° and dip angle SW 65°. F15 is about 1100 m, located in west showing a reverse fault, with the strike NE 34° and dip angle NW 65° (Fig. 2).

There coexist iron ores and magnesite ores in Lilaozhuang deposit. The iron ores in the Lilaozhuang deposit show mainly silicate, carbonate, and quartz type, among which silicate type is the most developed. The silicate type consists of magnetite (or hematite), amphibole, and quartz, sometimes bearing small amounts of chlorite with banded structure (Fig. 4a, b). The carbonate type, occurs in the transition zone between the silicate-type iron ore and magnesite, is composed primarily of magnetite (or hematite), magnesite (iron–magnesite), and a small amount of siderite, containing a small amount of quartz with massive or disseminated structure, crystalloblastic texture (Fig. 4c, d). The quartz-type ore is less common in this region and locates at the top of the ore body. It is mainly comprised of magnetic (or hematite) and quartz, and possesses banded formation.

Magnesite ore bodies occur in the magnetite layer and magnesium-rich carbonate rocks at the top section of the Wuji Group. The ore bodies present as lenticular, and their dip and strike are consistent with the attitude of surrounding rocks, which is controlled by the Lilaozhuang syncline,

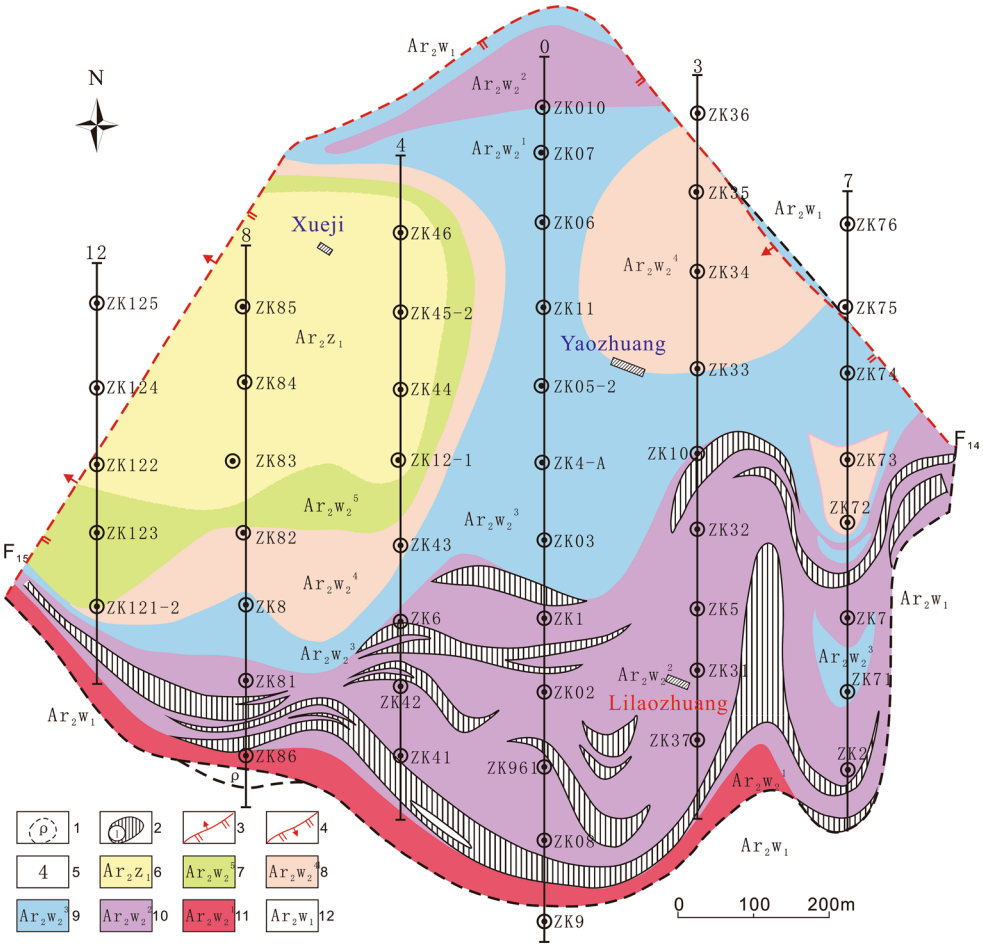

Fig. 2 Bedrocks geological sketch of the Lilaozhuang deposit in Huoqiu region (Presinian system) (Sun 2007). *1* Pegmatite; *2* ore body and its number; *3* speculated thrust fault and its number; *4* speculated normal faults and its number; *5* section line number; *6* migmatite gneiss in lower section of Zhouji formation; *7* upper schist with magnetite in upper section of Wuji formation; *8* upper migmatite in upper section of Wuji formation; *9* upper gneiss in upper section of Wuji formation; *10* lower magnetite with magnesium-rich carbonate in upper section of Wuji formation; *11* lower gneiss in upper section of Wuji formation; *12* banded migmatite in lower section of the Wuji formation

with strike is nearly EW and gradually becomes slow from bottom to top. The top and bottom of ore bodies are mainly dolomite marble, sandwiched mainly with serpentinite and magnesite dolomite marble. The ore is white or gray sparry magnesite (Fig. 4e), which is mainly composed of magnesite, and contains a small amount of dolomite, serpentine, phlogopite, and magnetite (hematite). Magnesite ore has prismatic porphyroblastic texture, and metasomatic texture does not develop well (Fig. 4f). Some magnesite ore presents as veined metasomatic dolomite or enveloped coarse magnesite or metasomatic fine magnesite. Ore structures present mainly as block structure, with a few banded, fine veins, and crushed structure.

Wall rock

The roof and bottom of iron–magnesite ore bodies at the Lilaozhuang area mainly contain plagioclase-bearing biotite quartz schist, and ore bodies are of the same occurrence. Their contacting boundary shows transition relationships because of containing magnetite. The interlayer substance of the ore bodies is mainly biotite quartz schist, biotite leptynite, and amphibolite rocks, secondly actinolite (Fe-bearing) schist, biotite plagioclase schist, hornblende plagioclase gneiss, magnesite-bearing dolomite marble. The surrounding rocks are generally lenticular, and a few are layered, with their dip and strike consistent with the attitude of the ore bodies. The contacting boundary between surrounding rocks and ore bodies is clear, except for a few presenting different transition relations due to the emergence of magnetite thin layer.

Biotite–quartz schist shows light brownish-black, often bearing chloritization features, with scaly granular crystalloblastic texture, and schistose structure. The rock has obvious schistosity and mainly consists of 60–65 wt% quartz, 30–35 wt% biotite and hornblende, small amounts of other minerals (±5 wt%), and occasional parallel-aligned garnet, quartz, hornblende between biotite (Fig. 5a). Leptynite shows brownish-black, chloritization develops obviously, with fine granular crystalloblastic texture and massive structure. The rock consists of 30–35 wt% quartz, 50 wt% feldspar, biotite 15–20 wt% (mostly chloritization), and sometimes a small amount of muscovite and amphibole (Fig. 5b). Plagioclase amphibolite shows dark green color, having columnar granular crystalloblastic texture and schistose structure, and some presenting sesame-like

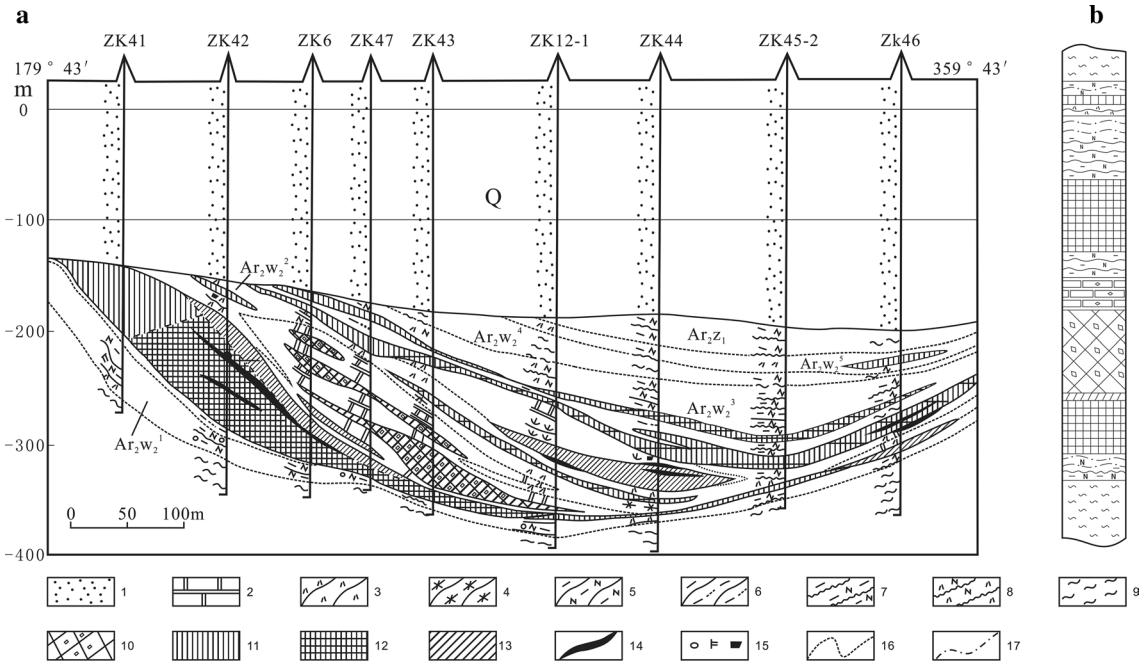

Fig. 3 Geological section of no. 4 exploration line in the Lilaozhuang deposit. *1* Quaternary; *2* dolomite marble with magnesite; *3* plagioclase amphibolite; *4* actinolite schists; *5* plagioclase biotite schist; *6* biotite quartz schist; *7* biotite plagioclase gneiss; *8* hornblende plagioclase gneiss; *9* migmatite; *10* magnesite; *11* quartz-type iron ore; *12* silicate-type iron ore; *13* carbonate-type iron ore; *14* rich iron ore body; *15* garnet, kyanite, and magnetite mineralization; *16* geological boundary; *17* oxidized and primary ore boundaries

dot structure or massive structure. The main mineral component is 50–85 wt% hornblende, 20–50 wt% plagioclase, and <5 wt% quartz (Fig. 5c, d).

Sample collection and analysis methods

All testing samples in this research are selected from drill core. Analysis on major elements, trace elements, as well as rare earth elements (REE), is performed on six iron ore samples, four magnesite samples, and seven wall-rock samples from Lilaozhuang deposit. In addition, C–O isotope measurements are taken on four magnesite samples and three carbonate rock samples of carbonate-type magnetite ore. All the representative samples for further analysis are checked by thin section firstly, and only those without cracks and veins filling are kept. Then, these qualified samples are ground to 200 mesh or less. The testing and analysis work on rock powers are done at Institute of Geology and Geophysics, Chinese Academy of Sciences (IGG, CAS).

Major elements are measured by XRF-1500 X-ray fluorescence spectrometer with RSD = 0.1–1 %, and the content of FeO is measured by potassium permanganate standard solution and direct titration method. Samples for trace element and rare earth element measurements are prepared by acid-leaching method and determined by inductively coupled plasma mass spectrometry (ICP-MS) (Element, Finnigan MAT) with RSD < 2.5 %. C–O isotopes are analyzed by gas isotope ratio mass spectrometer MAT-252 with RSD < 0.2 ‰, the measurements are stable, and the test results are reproducible.

Results

Iron ore

The primary iron ore at the Lilaozhuang ore deposit is silicate type and carbonate type, with a small amount of quartz type. Three silicate-type and three carbonate-type ores are selected in this study for major elements, trace elements, and REE analysis, and the results are listed in Table 2. The TFe_2O_3 (all iron as Fe^{3+}) content in both silicate-type and carbonate-type iron ores is >30 wt% (30.51–61.49 wt%), with TFe_2O_3/FeO less ranging from 1.51 to 3.23, which indicates that both ores are primary ores. The P_2O_5 content is very low (0.01–0.07 wt%). The SiO_2 content in silicate type is a bit higher (32.79–44.60 wt%), containing relatively high TiO_2 and Al_2O_3 contents, and those mixing with a small amount of magnesite bear higher levels of MgO. The carbonate type nearly does not contain TiO_2, also with very low SiO_2 content (0.27–0.49 wt%), but contains higher content of MnO, MgO, and CaO.

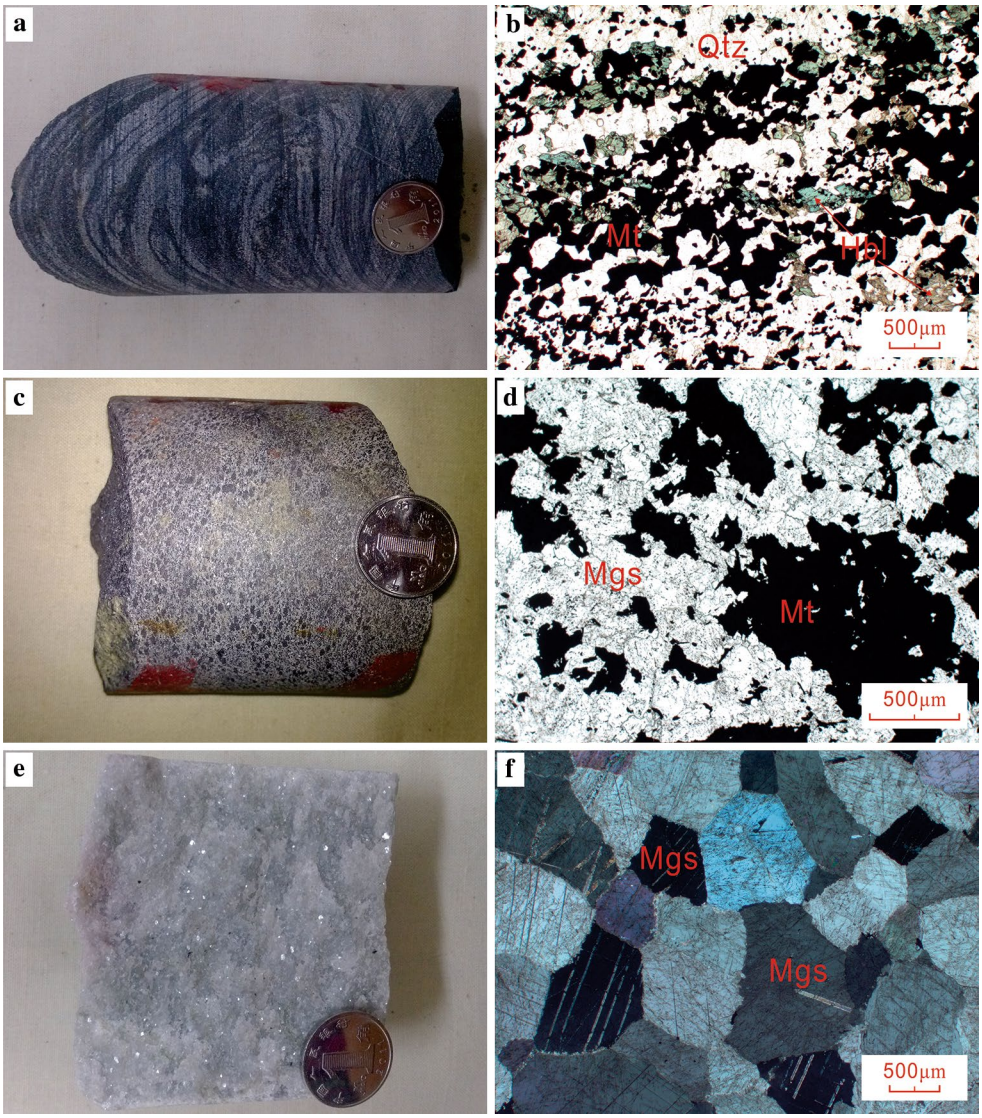

Fig. 4 Hand specimens and microscopic characteristics of the ore in Lilaozhuang deposit. **a** Banded iron ore, **b** silicate-type iron ore (−), **c** carbonate-type iron ore, **d** carbonate-type iron ore (−), **e** magnesite and **f** magnesite (−). *Qtz* quartz, *Hbl* hornblende, *Mt* magnetite, *Mgs* magnesite

The total rare earth elements and yttrium (ΣREY) content of the two types of ores at the Lilaozhuang ore deposit are low, with an average of 6.81 ppm (3.82–8.46 ppm). After normalizing REY in iron ore (Fig. 6a) by Post-Archean Australian Shale (PAAS) (McLennan 1989), the REE distribution pattern of the two types of ores is consistent, both showing enrichment in heavy rare earth elements, with $(La/Yb)_{PAAS}$ = 0. 12–0.36, and bearing distinctively positive anomalies in La (La/La* = 1.44–2.42) and significant strong positive anomalies in Eu (Eu/Eu* = 1.68–3.13) and Y (Y/Y* = 1.54–2.11). Quantification of anomalies in shale-normalized (Post-Archean Australian Shale, PAAS, from McLennan 1989) REY distribution patterns followed Bau and Dulski (1996): $La/La^* = La_{PAAS}/(3Pr_{PAAS} - 2Nd_{PAAS})$, $Ce/Ce^* = 2Ce_{PAAS}/(La_{PAAS} + Pr_{PAAS})$ (Bau and Dulski 1996), $Eu/Eu^* = Eu_{PAAS}/(0.67Sm_{PAAS} + 0.33Tb_{PAAS})$, $Y/Y^* = 2Y_{PAAS}/(Dy_{PAAS} + Ho_{PAAS})$, where PAAS indicates normalized concentration.

The trace element contents and distribution pattern of the two types of iron ores are similar on primitive mantle-normalized trace element partitioning map, showing strong negative anomalies in high field strength elements (HFSE) such as Nb, Ta, Zr, Hf, Ti (Fig. 6b), suggesting that metallogenic materials may be the same, which is typical of BIF sedimentary characteristics.

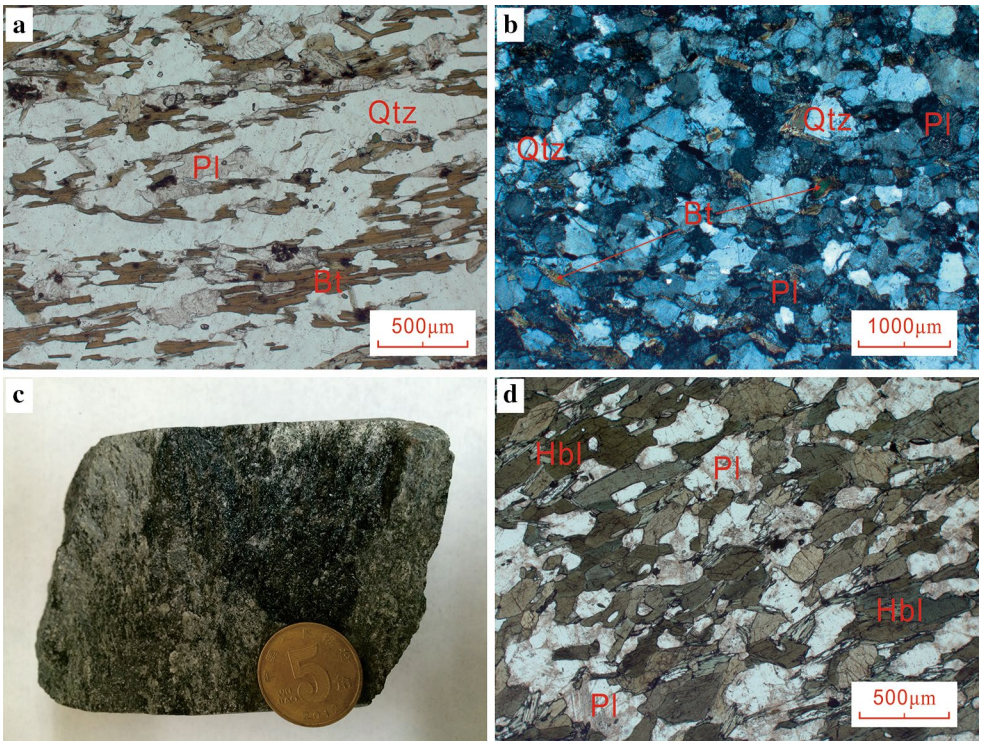

Fig. 5 Hand specimens and microscopic characteristics of the wall rocks in the Lilaozhuang deposit. **a** Biotite quartz schist (−), **b** Leptynite (+), **c** amphibolite; and **d** amphibolite (−). *Qtz* quartz; *Bt* biotite; *Pl* plagioclase, *Hbl* hornblende, *Mt* magnetite, *Mgs* magnesite

Magnesite ore

The magnesite ore at the Lilaozhuang ore deposit is associated with a small amount of siderite. The results of major and trace element analysis of four magnesite samples are listed in Table 3. It shows that the major oxide components in the magnesite are MgO and TFe_2O_3, which range from 40.87 to 44.15 wt% and 6.36 to 9.90 wt%, respectively. The iron occurs majorly in the form of Fe^{2+}. In addition to MgO and TFe_2O_3, the content of other oxides is very low. SiO_2 and CaO of most samples are <1 wt%, MnO of most samples ranges from 0.28 to 0.46 wt%, and other oxides are almost zero (TiO_2, Al_2O_3, Na_2O, K_2O, and P_2O_5). What is worth mentioning is that all of the magnesite ore samples have high losses on ignition (LOI) (more than 47 wt%).

The total REE content of magnesite is low with ΣREE = 5.20–5.78 ppm, showing positive anomalies in Eu (Eu/Eu* = 1.44–3.67) and Y (Y/Y* = 1.67–2.55) on PAAS-normalized REE distribution patterns. Light and heavy REEs show no clear fractionation with $(La/Yb)_{PAAS}$ = 1.05–1.92 (Fig. 6c). Magnesite shows strong negative anomalies in HFSE (Nb, Ta, Zr, Hf, Ti) and positive anomalies in large-ion lithophile elements (LILE) (K, Rb, Sr, Ba) on primitive mantle-normalized trace element partitioning map (Fig. 6d).

The results of C–O isotope measurement on pure magnesite and magnesite associated with magnetite are listed in Table 4. $\delta^{13}C$ in magnesite ranges between −1.362 and −2.159 ‰, which is higher than that of magnesite associated with magnetite (−5.30 to −10.66 ‰). $\delta^{18}O$ in magnesite varies in the range of 10.98–11.25 ‰, which is slightly lower than that of magnesite associated with magnetite (12.49–15.43 ‰). $\delta^{13}C$ and $\delta^{18}O$ values in all samples deviate from their normal values in marine carbonate.

Wall rock

The surrounding rock of the Lilaozhuang ore deposit is mainly biotite–quartz schist, leptynite, plagioclase amphibolite, and the major and trace element analysis results are shown in Table 5.

All of the biotite–quartz schist shows high contents of SiO_2 (more than 70 wt%), with Al_2O_3 is about 9 wt%, TFe_2O_3 is about 7 wt%, and very low content of other oxides (such as TiO_2, Al_2O_3, MgO, CaO, Na_2O, K_2O, and P_2O_5). The SiO_2 content in leptynite is about 60 wt%, Al_2O_3 is about 17 wt%, TFe_2O_3 ranges from 5.96 to 8.33 wt%, and the total content of other oxides is slightly higher than that in biotite quartz schist. The major oxide components in amphibolite are SiO_2 (about 40 wt%),

Table 2 Major (wt%) and trace (ppm) element contents of iron ores

Sample no.	LLZ-3	LLZ-7	LLZ-8	LLZ-11	LLZ-13	LLZ3-2	Sample Id	LLZ-3	LLZ-7	LLZ-8	LLZ-11	LLZ-13	LLZ3-2
Sample types	Silicate type			Carbonate type			Sample types	Silicate type			Carbonate type		
SiO_2	32.79	40.29	44.60	0.49	0.31	0.27	Pr	0.13	0.22	0.12	0.20	0.10	0.07
TiO_2	0.01	0.04	0.01	0.00	0.00	0.00	Nd	0.58	0.95	0.60	0.99	0.43	0.32
Al_2O_3	0.10	0.33	0.28	0.23	0.00	0.00	Sm	0.13	0.19	0.15	0.20	0.11	0.07
MnO	0.23	0.04	0.04	0.88	0.70	0.91	Eu	0.07	0.11	0.12	0.08	0.06	0.05
MgO	24.86	2.43	2.69	14.92	28.21	20.04	Gd	0.19	0.25	0.23	0.25	0.20	0.10
CaO	0.63	1.68	1.95	1.64	0.51	0.47	Tb	0.04	0.04	0.04	0.04	0.05	0.02
Na_2O	0.02	0.41	0.36	0.24	0.24	0.24	Dy	0.24	0.30	0.28	0.30	0.38	0.16
K_2O	0.01	0.04	0.04	0.00	0.04	0.00	Y	2.30	2.85	3.67	3.38	4.35	1.82
P_2O_5	0.01	0.07	0.04	0.07	0.04	0.04	Ho	0.05	0.07	0.07	0.09	0.10	0.04
FeO	13.12	18.14	17.10	24.09	20.80	14.93	Er	0.15	0.22	0.21	0.29	0.31	0.15
TFe_2O_3	30.51	55.79	51.96	61.49	31.44	48.26	Tm	0.02	0.03	0.03	0.04	0.04	0.02
LOI	10.81	−1.02	−1.56	20.36	39.34	29.92	Yb	0.18	0.24	0.21	0.34	0.30	0.19
TOTAL	99.98	100.08	100.41	100.32	100.83	100.15	Lu	0.04	0.04	0.03	0.06	0.05	0.03
Li	8.94	1.81	3.39	0.18	0.09	0.20	Hf	0.01	0.04	0.02	0.02	0.01	0.02
Be	0.54	0.15	0.41	0.03	0.05	0.02	Ta	0.01	0.00	0.00	0.00	0.01	0.00
Sc	24.34	25.13	18.14	0.21	32.65	0.21	Tl	0.00	0.00	0.00	0.00	0.00	0.02
V	5.39	8.79	6.17	2.35	6.10	1.84	Pb	0.23	1.08	4.96	0.17	0.11	0.65
Cr	168.62	307.09	283.05	12.00	342.30	45.98	Bi	0.01	0.02	0.02	0.02	0.01	0.11
Co	4.26	4.80	4.04	0.65	5.64	1.82	Th	0.07	0.19	0.06	0.04	0.04	0.08
Ni	94.04	89.09	98.01	4.03	158.31	15.38	U	0.11	0.08	0.04	0.05	0.03	0.20
Cu	1.34	0.70	3.12	1.24	0.42	4.65	Ti	67.29	235.60	58.83	0.00	0.00	0.00
Zn	15.62	8.71	21.56	3.92	1.74	5.89	∑REY	5.49	8.31	7.12	8.46	7.66	3.82
Ga	2.28	0.74	1.15	0.63	7.37	0.20	Y/Ho	43.64	39.12	53.40	38.40	42.17	42.15
Rb	0.78	0.68	0.79	0.11	0.33	0.20	La/La*	1.50	1.67	1.75	2.42	1.44	1.69
Sr	7.61	14.98	8.37	2.10	2.71	1.65	Pr/Pr*	1.02	1.00	0.98	1.01	1.18	1.04
Zr	0.43	1.06	0.29	1.10	0.31	1.10	Ce/Ce*	0.81	0.78	0.84	0.67	0.55	0.71
Nb	0.26	0.10	0.30	0.08	0.28	0.07	Eu/Eu*	2.14	2.53	3.13	1.75	1.68	3.13
Cs	1.16	0.40	0.04	0.03	0.04	0.03	Y/Y*	1.65	1.54	2.11	1.64	1.73	1.73
Ba	1.55	1.27	1.10	0.23	0.69	1.85	$(La/Yb)_{PAAS}$	0.20	0.36	0.16	0.20	0.12	0.13
La	0.50	1.13	0.47	0.93	0.48	0.32	Sr/Ba	4.92	11.79	7.58	9.10	3.93	0.89
Ce	0.88	1.68	0.88	1.26	0.70	0.46	Ti/V	12.49	26.81	9.54	0.00	0.00	0.00

$La/La^* = La_{PAAS}/(3Pr_{PAAS} - 2Nd_{PAAS})$; $Ce/Ce^* = 2Ce_{PAAS}/(La_{PAAS} + Pr_{PAAS})$ (Bau and Dulski 1996); $Eu/Eu^* = Eu_{PAAS}/(0.67Sm_{PAAS} + 0.33Tb_{PAAS})$ (Bau and Dulski 1996); $Y/Y^* = 2Y_{PAAS}/(Dy_{PAAS} + Ho_{PAAS})$; standardized data are cited from McLennan (1989)

TFe_2O_3 (about 19 wt%), Al_2O_3 (about 13–14 wt%), and CaO (about 10 wt%), the other oxide contents, such as MgO, K_2O, Na_2O, P_2O_5, and TiO_2, are generally low.

The average of total REE (ΣREE) content in biotite–quartz schist is 89.58 ppm, with average of $(La/Yb)_N$ being 24.58. There is a significant enrichment in light rare earth elements (LREE) on chondrite-normalized REE distribution patterns (Fig. 6e). The total content of REE (ΣREE) in leptynite varies from 72.16 to 122.27 ppm, with an average of 97.44 ppm, and $(La/Yb)_N$ varies from 8.46 to 25.78, with an average of 16.09, showing significantly enrichment in LREE. The average of total content of REE in amphibolite is 56.13 ppm, and differentiation of LREE is not obvious (Fig. 6e). All samples do not show distinct anomaly in Ce and Eu.

Biotite quartz schist is strongly depleted of Ba, Nb, Ta, Ti, Ce, Sr on the primitive mantle-normalized pattern map, but enriched in U, La, Pb, Nd, Cs, Gd, LREE. Leptynite is depleted of Th, Nb, Ta, Ce, P, Ti, enriched in Ba, U, La, Pb, Sr, Nd, Gd, LREE. Both show clastic sediment features. Plagioclase amphibolite shows depletion of Th, U, Nb, Sr, enrichment of Rb, Ta, Pb, Nd, Cs (Fig. 6f), which is typical of volcanic sediment.

Judging from the diagram for protolith reconstruction (Fig. 7), the protolith of biotite quartz schist at the

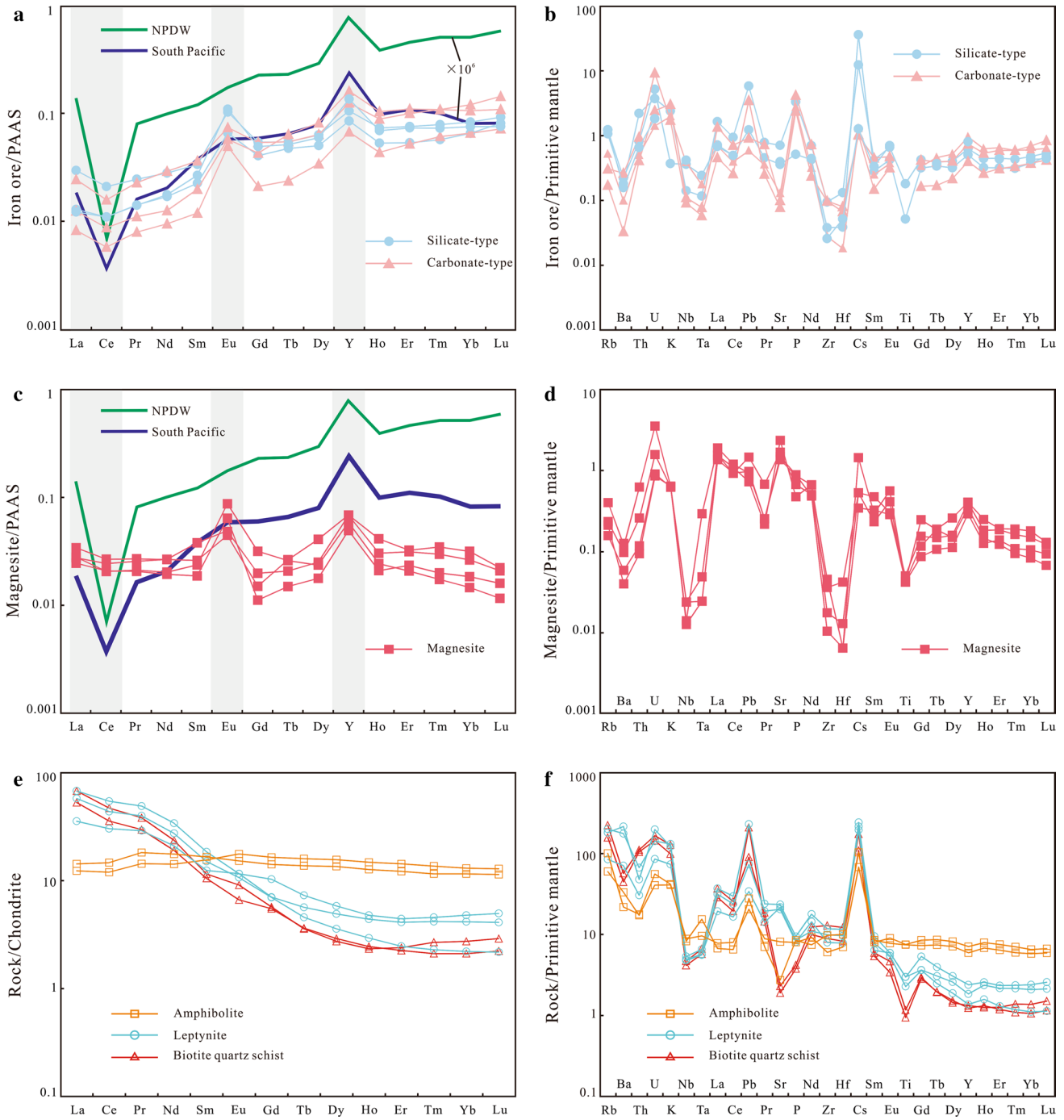

Fig. 6 PAAS, chondrite, and primitive mantle-normalized REE and trace elements patterns of iron ores, magnesites, and wall rocks in the Huoqiu iron deposit. PAAS normalization values are from McLennan (1989). The values of the chondrite are after Taylor and McLennan (1985). Primitive mantle normalization values are from Sun and McDonough (1989). NPDW—seawater at 2500 m in the North Pacific; South Pacific—average values at 0, 9, and 30 m in South Pacific (Bau and Dulski 1999)

Table 3 Major (wt%) and trace (ppm) element contents of magnesites

Sample no.	13LLZ-9	13LLZ-12	13LLZ-16	13LLZ-24	Sample no.	13LLZ-9	13LLZ-12	13LLZ-16	13LLZ-24
Sample types	Magnesite				Sample types	Magnesite			
SiO_2	0.44	0.85	1.02	0.82	Ba	2.19	0.68	0.41	0.28
TiO_2	0.00	0.01	0.00	0.00	La	1.06	0.70	0.87	0.93
Al_2O_3	0.01	0.04	0.08	0.02	Ce	1.63	1.29	1.41	1.65
MnO	0.28	0.45	0.46	0.34	Pr	0.19	0.15	0.16	0.18
MgO	44.15	41.26	40.87	42.12	Nd	0.69	0.60	0.60	0.65
CaO	0.87	0.88	0.87	0.87	Sm	0.13	0.14	0.10	0.10
Na_2O	0.00	0.00	0.00	0.00	Eu	0.09	0.05	0.05	0.07
K_2O	0.01	0.01	0.01	0.01	Gd	0.15	0.09	0.07	0.05
P_2O_5	0.01	0.01	0.01	0.01	Tb	0.02	0.02	0.02	0.01
FeO	4.95	7.86	7.81	5.20	Dy	0.11	0.12	0.19	0.08
TFe_2O_3	6.36	9.90	9.87	7.62	Ho	0.02	0.03	0.04	0.02
LOI	48.54	47.36	47.26	48.47	Er	0.06	0.09	0.09	0.07
TOTAL	100.68	100.77	100.45	100.28	Tm	0.01	0.01	0.01	0.01
Li	1.34	1.07	1.68	1.65	Yb	0.04	0.07	0.09	0.05
Be	0.07	0.07	0.08	0.06	Lu	0.01	0.01	0.01	0.01
Sc	0.08	0.03	0.33	0.44	Hf	0.00	0.00	0.00	0.01
V	0.17	0.06	0.08	0.20	Ta	0.00	0.00	0.01	0.00
Cr	8.33	7.11	7.31	8.37	Tl	0.00	0.00	0.00	0.00
Co	27.36	28.13	25.40	28.21	Pb	0.27	0.13	0.17	0.18
Ni	7.48	6.28	2.42	2.19	Bi	0.01	0.01	0.00	0.00
Cu	0.98	0.49	1.16	1.71	Th	0.05	0.02	0.01	0.01
Zn	2.25	9.14	3.51	4.29	U	0.07	0.03	0.02	0.02
Ga	0.28	0.35	0.22	0.21	ΣREY	4.21	3.35	3.71	3.89
Rb	0.26	0.15	0.10	0.13	Pr/Pr*	1.03	1.00	1.01	1.03
Sr	35.46	49.53	28.60	31.20	Ce/Ce*	0.84	0.92	0.87	0.92
Y	1.58	1.83	1.85	1.33	La/La*	1.22	1.18	1.23	1.06
Zr	0.12	0.20	0.51	0.40	$(La/Yb)_{PAAS}$	1.92	1.05	1.08	1.33
Nb	0.02	0.02	0.01	0.01	Eu/Eu*	3.58	1.44	1.70	3.67
Cs	0.05	0.02	0.01	0.02	Y/Y*	2.45	2.46	1.67	2.55

$La/La^* = La_{PAAS}/(3Pr_{PAAS} - 2Nd_{PAAS})$; $Ce/Ce^* = 2Ce_{PAAS}/(La_{PAAS} + Pr_{PAAS})$ (Bau and Dulski 1996); $Eu/Eu^* = Eu_{PAAS}/(0.67Sm_{PAAS} + 0.33Tb_{PAAS})$ (Bau and Dulski 1996); $Y/Y^* = 2Y_{PAAS}/(Dy_{PAAS} + Ho_{PAAS})$; standardized data are cited from McLennan (1989)

Table 4 Results of C–O isotopes of magnesites

Sample no.	Rock/mineral	δ13C ‰ (PDB)	δ18O ‰ SMOW
LLZ-11	Carbonate	−10.66	14.52
LLZ-13		−5.30	12.49
LLZ3-2		−6.76	15.43
13LLZ-9	Magnesite	−1.35	10.98
13LLZ-12		−2.04	11.25
13LLZ-16		−1.36	11.11
13LLZ-24		−2.16	11.24

Lilaozhuang orefield is clay rock or mud shale, the protolith of leptynite is sandy rock or graywacke, and the protolith of amphibolite should be tholeiitic basalt.

Discussion

Material sources

According to Sang et al. (1981), most Huoqiu BIF samples have initial $^{87}Sr/^{86}Sr$ values between 0.704 and 0.707, which are a little higher than that of the initial value of upper mantle (0.703) and above the continental crust growth curve. This indicates that the original substances of metamorphic rocks of the Huoqiu Group is not from upper mantle directly, but has been affected by continental crust. However, because the initial $^{87}Sr/^{86}Sr$ value is less than that of normal continental crust (0.719), this shows that the protolith is not entirely from sialic continental crust rocks. These features indicate neither the ore deposit is simply

Table 5 Major (wt%) and trace (ppm) element contents of surrounding rocks

Sample no.	LLZ-9	LLZ-10	LLZ-12	LLZ3-7	LLZ3-9	13LLZ-28	LLZ2-6	Sample no.	LLZ-9	LLZ-10	LLZ-12	LLZ3-7	LLZ3-9	13LLZ-28	LLZ2-6
Sample types	Biotite quartz schist		Leptynite			Amphibolite		Sample types	Biotite quartz schist		Leptynite			Amphibolite	
SiO_2	73.55	75.52	57.31	60.52	57.36	41.86	40.99	Cs	5.52	3.46	6.83	7.67	6.16	2.16	3.28
TiO_2	0.25	0.20	0.63	0.48	0.63	1.58	1.59	Ba	394.06	309.23	1217.52	1489.33	489.66	230.71	151.71
Al_2O_3	9.84	8.14	17.25	16.67	17.49	13.59	13.61	La	25.16	19.68	25.20	21.45	13.25	5.35	4.61
MnO	0.11	0.09	0.12	0.06	0.06	0.32	0.32	Ce	45.12	34.27	52.30	41.97	29.18	14.18	11.57
MgO	2.54	2.60	3.48	4.13	5.79	9.27	9.32	Pr	5.13	3.98	6.57	5.34	3.89	2.45	1.93
CaO	0.55	1.11	2.76	2.58	2.03	10.05	10.08	Nd	16.71	13.47	24.04	19.38	14.82	12.47	10.08
Na_2O	0.13	0.14	3.67	2.93	4.17	1.18	1.16	Sm	2.63	2.39	4.21	3.43	2.83	3.78	3.54
K_2O	3.75	2.88	3.82	3.52	2.13	1.20	1.22	Eu	0.78	0.57	0.99	0.92	1.00	1.31	1.51
P_2O_5	0.09	0.08	0.20	0.17	0.18	0.17	0.18	Gd	1.76	1.70	3.18	2.16	2.17	4.35	5.07
FeO	5.44	5.00	6.00	4.59	5.51	12.67	13.28	Tb	0.21	0.21	0.43	0.27	0.33	0.80	0.93
TFe_2O_3	7.42	6.65	8.33	5.96	7.23	18.67	19.18	Dy	1.06	1.13	2.26	1.39	1.91	5.23	6.03
LOI	2.04	2.66	1.98	2.72	2.74	2.02	1.96	Ho	0.21	0.22	0.42	0.26	0.39	1.12	1.30
TOTAL	100.27	100.07	99.55	99.74	99.81	99.91	99.61	Er	0.61	0.57	1.13	0.63	1.04	3.08	3.61
Li	49.20	60.52	58.26	75.90	80.68	34.26	42.66	Tm	0.10	0.08	0.18	0.09	0.16	0.44	0.52
Be	0.90	0.73	1.17	1.10	0.82	0.64	3.66	Yb	0.68	0.52	1.18	0.55	1.03	2.85	3.22
Sc	4.81	4.13	13.78	8.16	11.01	43.33	53.17	Lu	0.11	0.09	0.19	0.08	0.16	0.44	0.49
V	33.68	30.06	120.84	70.13	132.25	212.36	326.79	Hf	3.77	2.55	3.57	2.42	2.98	2.16	3.09
Cr	262.00	236.66	163.84	146.30	138.30	149.76	96.51	Ta	0.27	0.24	0.27	0.23	0.23	0.39	0.63
Co	9.89	10.26	25.96	14.18	21.40	56.62	60.25	Tl	0.49	0.32	0.53	0.56	0.33	0.18	0.23
Ni	22.88	22.02	43.80	40.31	48.78	91.90	75.71	Pb	16.52	38.29	42.13	13.46	6.26	3.78	5.12
Cu	32.53	42.06	217.91	9.02	12.30	176.01	6.94	Bi	0.38	0.45	0.12	0.07	0.05	0.02	3.94
Zn	16.86	33.14	171.82	60.89	66.11	111.76	98.21	Th	9.32	8.81	5.64	4.04	2.58	1.46	1.50
Ga	12.68	11.77	19.32	18.89	18.46	19.06	18.37	U	3.45	3.01	2.96	4.12	1.78	0.85	1.16
Rb	140.83	99.02	125.37	113.88	53.30	37.68	63.17	ΣREE	100.27	78.89	122.27	97.89	72.16	57.84	54.42
Sr	48.79	40.16	492.37	429.14	455.34	171.30	57.78	Ce/Ce*	0.89	0.86	0.93	0.90	0.94	0.90	0.90
Y	6.04	5.64	10.89	6.25	8.41	26.95	32.22	Eu/Eu*	1.06	0.83	0.80	0.97	1.19	0.99	1.10
Zr	144.17	99.46	131.69	89.02	110.93	67.45	108.91	$(La/Yb)_N$	24.41	24.75	14.02	25.78	8.46	1.23	0.94
Nb	3.34	2.95	3.82	3.40	3.50	6.30	5.87								

Note that the data of LLZ-9, LLZ-10, LLZ-12, LLZ3-7, and LLZ-11 are from Huang et al. (2013)

$Ce/Ce^* = 2Ce_N/(La_N + Pr_N)$; $Eu/Eu^* = 2Eu_N/(Sm_N + Gd_N)$; the values of the chondrite are after Taylor and McLennan (1985)

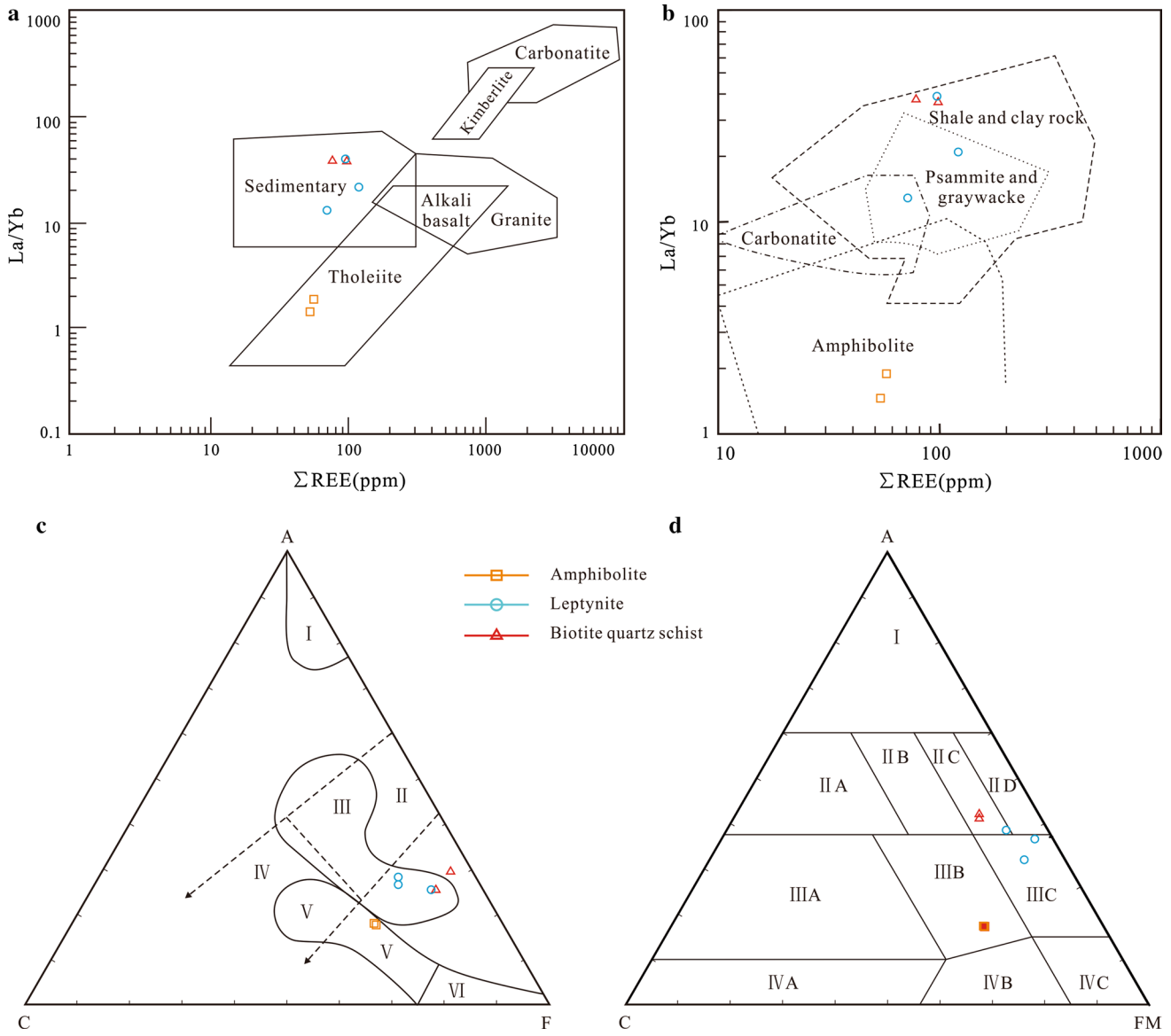

Fig. 7 Diagrams for protolith reconstruction. **a**, **b** Discriminant diagram of La/Yb −ΣREE, after Zhao (1997). **c** Discriminant diagram of A–C–F. A = Al_2O_3 + $Fe_2O_3^-$ (Na_2O + K_2O), C = CaO, F = FeO + MgO + MnO, A + C + F = 100, I—aluminum-rich clays and shales, II—clays and shales (including 0–35 % carbonate content), III—graywacke, IV—marl (including 35–65 % carbonate), V—basaltic rocks and andesitic rocks, VI—ultramafic rocks. **d** Discriminant diagram of A–C–FM. A = $Al_2O_3/\Sigma \times 100$, C = $CaO/\Sigma \times 100$, F = $(FeO + 2Fe_2O_3)/\Sigma \times 100$, M = $MgO/\Sigma \times 100$, $\Sigma = Al_2O_3 + CaO + FeO + 2Fe_2O_3 + MgO$, A + C + F + M = 100, I—clay and acidic volcanic rock, IIA—feldspathic sandstone, IIB—neutral–acidic volcanic rocks, IIC—neutral–acidic volcanic rocks and graywacke, IID—clay rocks and graywacke, IIIA—lime silicate and quartzite, IIIB—mafic volcanic rocks and magnesia dolomitic marl, IIIC—tuffaceous siltstone, IVA—calcium carbonates, IVB—ultrabasic rocks, IVC—ferrosilicon sedimentary rocks + ultrabasic rocks

formed by volcanic processes, nor is from terrestrial sentiment, but is from both and has a volcanic sedimentary genesis.

The TiO_2 and Al_2O_3 contents of iron ore are low within the range of 0–0.37 wt% and have an average of 0.17 wt%. The HFSE shows strong depletion on trace element spider diagram (Fig. 6b) and implies small amount of terrestrial materials is added in the BIF deposition process (Basta et al. 2011; Lan et al. 2014; Pecoits et al. 2009).

Modern oxidized seawater is characterized by positive anomaly in La, Gd, and Y, and negative anomaly in Ce. Compared with HREE, LREE and MREE are relative depleted (Fig. 6a, c). When compared to the low-temperature hydrothermal fluid (<250 °C), the seafloor

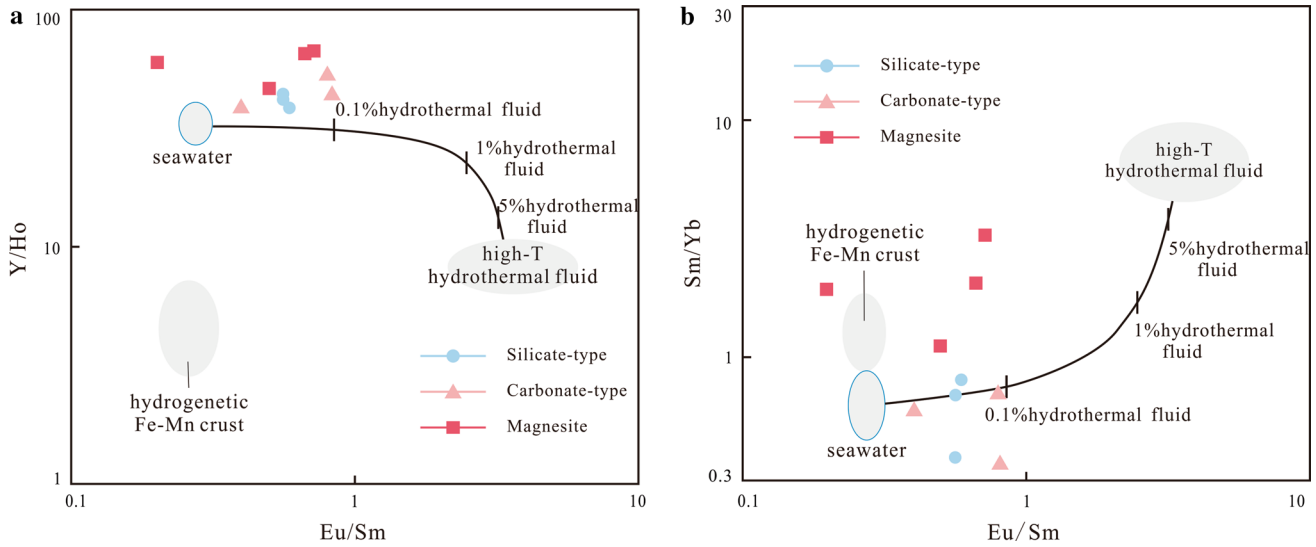

Fig. 8 Y/Ho–Eu/Sm (**a**), Sm/Yb–Eu/Sm (**b**) diagrams of iron ores and magnesites (Alexander et al. 2008)

high-temperature hydrothermal (>250 °C) has obvious positive anomaly in Eu ($Eu/Eu_{PAAS}^* > 1$) and large $(Sm/Yb)_{PAAS}$ (Bau and Dulski 1999; Bolhar et al. 2004; Bolhar and Van Kranendonk 2007). Alibo and Nozaki (1999) also suggested that modern seawater shows characteristics of enrichment in HREE, and positive anomaly in La and Y on PAAS-standardized REE distribution patterns. The positive anomaly in Eu characterizes the seafloor hydrothermal activity (Bau and Dulski 1996; Danielson et al. 1992; Douville et al. 1999) and is often considered as signs of participation of high-temperature hydrothermal fluids (Murray et al. 1991).

REEs are one of the most useful geochemical tools when studying the source of BIFs with the assumption that there is minimal fractionation of REEs during the precipitation of ferric iron oxides and oxyhydroxides (Bekker et al. 2010). Bau (1993) indicated that Precambrian BIFs were generally not affected by relatively low degrees of metamorphism and low fluid/rock conditions during metamorphism. The Y/Ho ratio value of seawater is about 44–74 and decreases with increasing depth, while terrestrial rocks and chondrites have a constant Y/Ho value of 26. In addition, the ratio of ocean ridge hydrothermal fluids ranges from 28 to 39 (Bau and Dulski 1999; Bolhar et al. 2004). The Sr/Ba ratio value of volcanic rocks and marine sediments is >1, while terrigenous sedimentary is <1 (Shen et al. 2009).

The Lilaozhuang BIF underwent low amphibolite facies metamorphism (Yang et al. 2014) and shows REE + Y patterns (Fig. 6a) similar to those of scarcely metamorphosed Precambrian BIFs (e.g., Alexander et al. 2008; Planavsky et al. 2010). Hence, the Lilaozhuang BIF likely preserves the original REE signatures of ambient seawater at the site of iron precipitation. Specifically, the PAAS-normalized REE + Y patterns of the Lilaozhuang BIF are depleted in LREEs with positive La and Y anomalies (Fig. 6a) and super chondritic Y/Ho ratios (38.40–53.40), which is consistent with the REE features of modern seawater (Alibo and Nozaki 1999) and suggests its deposition in seawater. In addition, a striking feature for all of the REE + Y patterns is that they display strongly positive Eu anomalies ($Eu/Eu^* = 1.68–3.13$), which can be attributed to the spreading-related high-temperature hydrothermal solutions expelled at the seafloor (Bau and Dulski 1999; Douville et al. 1999). It is generally assumed that Fe and REEs do not fractionate during transport from spreading or other exhalative centers (Bekker et al. 2010). The average of Sr/Ba is 6.37, suggesting mineralization at Lilaozhuang is related with volcanism and BIF iron ore is deposited from mixed solutions Alibert and McCulloch 1993; Bau et al. 1997; Khan et al. 1996. Combining with the chemical signatures commonly observed in the Precambrian BIFs (Bau and Dulski 1999; Bekker et al. 2010; Bolhar et al. 2005; Klein 2005), we propose that the Lilaozhuang BIF was precipitated from marine seawater with high-temperature hydrothermal fluids. Furthermore, Alexander et al. (2008) introduced a two-component mixing model to detect the proportion of seawater and high-temperature hydrothermal fluids in the original mixture. According to the Sm/Yb–Eu/Sm diagram, extremely small quantities of high-temperature hydrothermal fluids (<0.1 %) were sufficient to yield strongly positive Eu anomalies in the Lilaozhuang BIF (Fig. 8a, b).

Depositional environment

Metasedimentary rock series can be used to judge sedimentary environment. There are two types of metamorphic

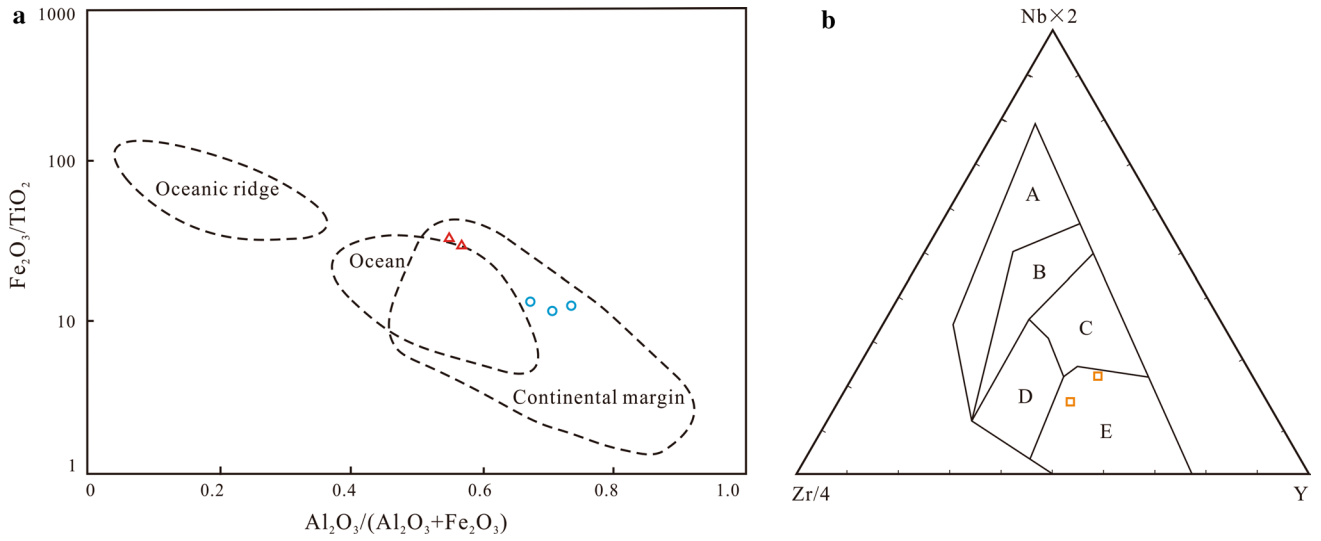

Fig. 9 Diagrams for discriminating tectonic environment. **a** Tectonic environment of biotite quartz schist and leptynite (Murray et al. 1991). **b** Tectonic environment of amphibolite (*A* within-plate alkaline basalts, *B* within-plate alkaline basalts, and within-plate tholeiites, *C* E-type MORB, *D* within-plate tholeiites and volcanic-arc basalts, *E* N-type MORB and volcanic-arc basalts) (Meschede 1986)

rocks coexisting at the Lilaozhuang ore deposit. Orthometamorphite, mainly consists of amphibolite transformed from metamorphic basalt, is dominated by plagioclase amphibolite. Parametamorphite is primarily composed of mica–quartz schist converted from argillaceous and sandy rock, as well as leptynite, gneiss that metamorphosed from psammite and graywacke; and secondly comprised of dolomitic marble transformed from dolomitic limestone. The discrimination on tectonic environment of biotite quartz schist and leptynite indicates that the Lilaozhuang ore deposit is formed on continental margin that is close to the deep ocean (Fig. 9a), and the discrimination on plagioclase amphibolite shows its formation environment is related to volcanic activity (Fig. 9b). Yang et al. (2014), Liu and Yang (2015) suggest that Huoqiu orefield is in the back-arc basin that located among Dangshan ancient land and Yinxianji volcanic island arc. There exist a lot of clastic and argillaceous materials accumulated in the back-arc basin that is close to the continental margin, which may provide sedimentary sources for the Lilaozhuang ore deposit, and later convert into biotite quartz schist, plagioclase amphibolite schist, gneiss, or leptynite. Our study is consistent with their conclusions, and the authors infer that the Lilaozhuang ore deposit may form on the active zone of back-arc basin close to the edge of the shallow sea.

Studies have shown that rock formed in mid-oceanic ridge and deep-sea plain is depleted in LREE, while rock formed in basin rifting phase and residual sea stage has rather obvious characteristics of LREE enrichment because it is close to the continent and hence strongly influenced by terrestrial sources (Armstrong et al. 1999). All the surrounding rock samples do not show apparent Ce anomaly (Ce/Ce* = 0.86–0.94, average is 0.90) and Eu anomaly (Eu/Eu* = 0.8–1.19, average is 0.97). Chondrite-normalized REE distribution patterns of biotite quartz schist and leptynite show significant LREE enrichment, but plagioclase amphibolite does not have significant LREE and HREE differentiation characteristics. These suggest Lilaozhuang ore deposit forms in rift basin or residual basin that is close to continental margin.

The Lilaozhuang ore deposit contains great amounts of magnesite and magnesium-rich carbonate rocks. Carbonate deposition distributes mainly in low-latitude shallow marine continental shelf and littoral regions without river filling. Carbonate deposition suffers from exclusion and disturbance in shallow basins with terrestrial input, and forms impure muddy and sandy carbonate rocks. Magnesium-rich carbonates and dolomites always form in barrier lagoons and bays because of the concentration of Mg^{2+} in seawater. In addition, the iron ore body centers on magnesite (magnesium-rich carbonate rock section) with some symmetry in the up and down direction. Meanwhile, there also exists phase transition relationship among magnesia marble–plagioclase amphibolite (actinolite–iron-bearing schist), mica schist, and leptynite (gneiss) in three-dimensional space. Though the thickness of rock sections varies widely, the layers are relatively stable and continuous (Fig. 3b). Therefore, the occurrence environment of the Lilaozhuang ore deposit may be sedimentary basin, with evolution features of changing from magnetite sub-facies to magnesium-rich carbonate sub-facies from the basin edge to the center. Magnetite sub-facies turn into magnetite and magnesium-rich carbonate sub-facies firstly, and then magnetite disappears and magnesium-rich carbonate sub-facies

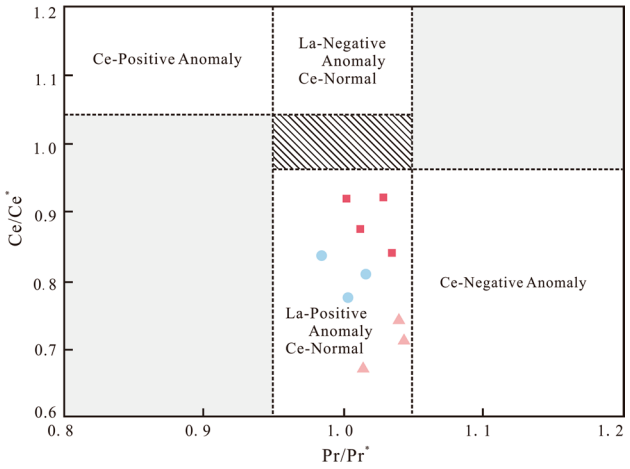

Fig. 10 Ce/Ce* versus Pr/Pr* discrimination diagram of iron ores and magnesites (Bau and Dulski 1996)

form in iron–magnesite monomineralic rock. Correspondingly, the iron content in iron magnetite becomes depleted, while magnesium enriched. According to the location of the sedimentary facies in the basin, this distribution pattern is related with the water depth of the basin, which causes different redox conditions, and carbonate abundance in different parts of the basin. The oxidation potential in the basin edge is higher than that in the center, while carbonate is relatively enriched in the center, which may be the product of lagoon or semi-enclosed basin.

TFe_2O_3/FeO of iron ore at the Lilaozhuang deposit is <3.5, in the range of 2.6–3.19, and the ferrous iron content in various types of surrounding rocks is very high, about 75 % in the total iron. In addition, it does not show negative Ce anomaly (Fig. 10) in the Pr/Pr* − Ce/Ce* discrimination diagram, indicating that the deposit formation environment is relatively lacking oxygen (Alibo and Nozaki 1999; Bau 1995; Zhang and Nozaki 1996). Hence, it can be concluded that the Lilaozhuang ore deposit is formed in low-oxygen fugacity reducing environment.

In summary, this paper speculates that the Lilaozhuang ore deposit may originate from a closed or semi-enclosed anoxic limitary marine back-arc basin that is close to the continental margin, which is likely to be a semi-enclosed basin.

Ore-forming processes

Combining with previous researches, this paper summarizes the characteristics of Lilaozhuang deposit. First, the iron ore and magnesite ore occur simultaneously, and appear with carbonate-type BIF. Second, the ore bodies are mainly stratiform-like, and some is lenticular. The stable layers have a conformable and clear contact with surrounding rocks, and their occurrence is identical. Third, there are a large amount of magnesium-rich carbonate rocks, mainly in the form of dolomitic marble, probably including some ferrodolomite. Fourth, the mineral and chemical composition of the iron ore and magnesite is relatively simple. Finally, the surrounding rocks are roughly equivalent to transgressive deposits of clast, clay, iron, and magnesium carbonate rock, magnesium-rich carbonate, which experience regional metamorphism that metamorphoses the whole set of rocks. The representative essential components of metamorphic rocks are biotite, hornblende, microcline, quartz, and a small amount of distinctive minerals in metamorphic process (e.g., garnet), indicating that the mineralization stage has undergone low-amphibolite-facies-equivalent regional metamorphism. The metamorphism in ore deposit is evident, such as bending schistosity, folding metamorphic bands, crushed, stretched, and differentially orientated minerals. According to these characteristics, we suggest that the Lilaozhuang deposit is sedimentary and metamorphic.

Diagenesis, metamorphism, and hydrothermal alteration after carbonate sedimentation all cause isotope fractionation, usually result in decreasing $\delta^{13}C$ and $\delta^{18}O$ (Banner and Hanson 1990; Bekker et al. 2001, 2005; Chen et al. 2000; Jiang et al. 2004; Ray et al. 2003; Veizer et al. 1999), with $\delta^{18}O$ changes more than $\delta^{13}C$ (Banner and Hanson 1990). Veizer et al. (1999) suggest that after carbonate precipitation, diagenesis can lead to decrease in $\delta^{18}O$ by an average of about 2 ‰. Schidlowski et al. (1975) hold that $\delta^{18}O$ value of metamorphosed or recrystallized carbonate rocks is lower than non-metamorphosed by 2–3 ‰, and there also exists isotope exchange between carbonates and organic materials during metamorphic process, resulting in lower $\delta^{13}C$ in carbonates and relative higher $\delta^{13}C$ in organic materials. Studies have shown that carbon and oxygen isotope values have inverse relation with metamorphic level. There is still minor ^{13}C in amphibolite facies carbonate, but none in granulite facies. Compared with amphibolite facies, the average $\delta^{13}C$ is lower by 5 ‰ or more, and reduction of $\delta^{18}O$ is >10 ‰ (Baker and Fallick 1989a, b; Melezhik et al. 2001a, b). Wada and Suzuki (1983) and Schidlowski (1988) found that metamorphism can lead to the reduction of $\delta^{13}C$ by greater than 3 ‰ when the temperature is higher than 650 °C.

To sum up, $\delta^{13}C$ and $\delta^{18}O$ values generally are decreasing in carbonate rocks in later geological processes (e.g., diagenesis and metamorphism). The average $\delta^{18}O$ in carbonate formations during global 2.33–2.06 Ga period is about 22 ‰, and in Precambrian dolomite (Archean and Paleoproterozoic) is 26 ± 2 ‰ (Veizer et al. 1992), so $\delta^{18}O$ in protolith of carbonate before Paleoproterozoic should be >22 ‰.

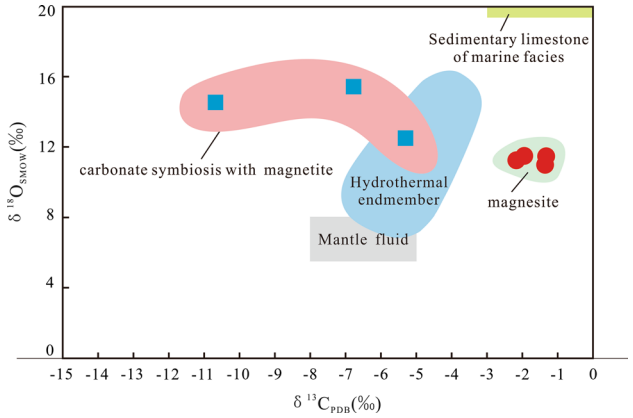

Fig. 11 C–O stable isotopes of carbonates in the Huoqiu BIF [The hydrothermal end member is from Stakes and O'Neil (1982)]

The $\delta^{18}O$ value in the Lilaozhuang magnesite sample is around 11 ‰, and $\delta^{18}O$ in carbonate associated with magnetite sample varies between 12.49 and 15.43 ‰, with an average of 14.15 ‰, showing strong depletion. It is far lower than $\delta^{18}O$ in general Precambrian marine carbonate (22 ‰) and is equivalent to amphibolite facies–granulite facies metamorphic grade. $\delta^{13}C$ and $\delta^{18}O$ values decrease simultaneously, $\delta^{13}C$ in magnesite sample, with an average of −1.73 ‰, is in the range of −2.16 to −1.35 ‰, while in carbonate associated with magnetite sample, averaged at −7.57 ‰, is −10.66 to −5.30 ‰. Both of them are lower than the average 0.5 ‰ of marine carbonate rocks (Schidlowski 1998), showing distinct negative anomalies. Because metamorphic grade at the entire Huoqiu orefield is low amphibolite facies (Yang et al. 2014), the decrease in $\delta^{18}O$ at the Lilaozhuang orefield cannot be sufficiently explained by metamorphism, and the impacts of hydrothermal fluids must be considered. Hydrothermal carbonates encompass a large array of value in $\delta^{13}C$, but more straight in $\delta^{18}O$ (Stakes and O'Neil 1982). Some indications have shown involvement of hydrothermal in metamorphic process of the ore deposits. Eu value presents significantly enrichment in ore, and followed by hydrothermal alteration features, such as K-feldsparization of plagioclase, biotitization of amphibole, cummingtonitization of hornblende, dissolution of siliceous strip, and the sequential metasomatic change in dolomite–magnesium siderite–iron magnesite–magnesite ore in carbonate rocks. The generation of disseminated ore and the emergence of serpentine also indicate that there exists gas–liquid metasomatic metamorphism in mineralization stage. Thin magnetite veins interspersed in the marble and magnesite also can be seen in the orefield. It does not form ore bodies with industrial significance; however, it is a sign of the participation of hydrothermal activities. Hence, hydrothermal fluid modification is one of the important reasons that change the C–O isotope system of magnesite and carbonate in Lilaozhuang besides later diagenesis and metamorphism.

The $\delta^{13}C$ and $\delta^{18}O$ of magnesite and carbonate associated with magnetite at Lilaozhuang are concentrated on two different ranges (Fig. 11). The $\delta^{13}C$ in carbonate symbiosis with magnetite is obviously lower than that in magnesite, while $\delta^{18}O$ is relatively higher, indicating their different forming mechanisms. This maybe because both of them have experienced the same metamorphism in their formation stage, but the formation of magnetite has clearly undergone more intense hydrothermal transforming effect.

In addition, the Lilaozhuang iron-bearing formation is located in the upper part of volcanic–sedimentary cycles of the Huoqiu Group. Based on the rock association, it is inferred that the deposit was formed at the stage when volcanism ended and normal sedimentation began. It can also be clearly shown from profile diagram (Fig. 3b) that the formation of iron and magnesite at the Lilaozhuang is mainly from sedimentation, with volcanic materials as minerogenetic basis and deposition material supplied primarily from terrestrial sources. It experiences diagenesis, metamorphism, and fluid reformation after deposition of rock-forming and ore-forming materials.

Conclusions

Based on regional and ore geologies, combining microscopic characteristics and geochemical characteristics of the ores and wall rocks, the author draws the following conclusions: (1) The protolith of surrounding rocks at the Lilaozhuang deposit is mainly composed of argillaceous, carbonate rocks, and a small amount of volcanic rocks. (2) The Lilaozhuang magnetite–magnesite deposit is formed in a semi-enclosed basin with low-oxygen and reducing environment related to the continental margin. The ore-forming materials are derived mainly from mixed solution of seawater and seafloor hydrothermal. (3) The Lilaozhuang deposit experiences complex evolution processes. The iron ores and magnesium-rich carbonates are deposited firstly in submarine setting and then are transformed by metamorphic fluids during regional metamorphism.

Acknowledgments The authors thank Prof. Yang Xiaoyong and 313 geological team from Bureau of Geology and Mineral Resources Exploration of Anhui Province for supporting and guiding in the fieldwork. We thank Dr. Zhu Mingtian for discussion and guidance in writing this paper. Measurements and tests are carried out by rock and mineral analysis laboratory, trace elements laboratory, stable isotope laboratory at Institute of Geology and Geophysics, Chinese Academy of Sciences. This research was supported by the State Key Basic Research Development Program of China (2012CB416601) and the National Natural Science Foundation of China (NSFC; grant numbers 41572076).

References

313 Geological Team (1991) Report of regional 1:50,000 geological survey in the Huoqiu iron ore field

313 Geological Team (1995) A final report of the Huoqiu iron ore field. Anhui Bur Geol Miner Resour (2):1–120

Alexander BW, Bau M, Andersson P, Dulski P (2008) Continentally-derived solutes in shallow Archean seawater: rare earth element and Nd isotope evidence in iron formation from the 2.9 Ga Pongola Supergroup, South Africa. Geochim Cosmochim Acta 72(2):378–394

Alibert C, McCulloch MT (1993) Rare earth element and neodymium isotopic compositions of the banded iron-formations and associated shales from Hamersley, Western Australia. Geochim Cosmochim Acta 57(1):187–204

Alibo DS, Nozaki Y (1999) Rare earth elements in seawater: particle association, shale-normalization, and Ce oxidation. Geochim Cosmochim Acta 63(3):363–372

Armstrong HA, Owen AW, Floyd JD (1999) Rare earth geochemistry of Arenig cherts from the Ballantrae Ophiolite and Leadhills Imbricate Zone, southern Scotland: implications for origin and significance to the Caledonian Orogeny. J Geol Soc 156(3):549–560

Baker AJ, Fallick AE (1989a) Evidence from Lewisian limestones for isotopically heavy carbon in two-thousand-million-year-old sea water. Nature 337(6205):352–354. doi:10.1038/337352a0

Baker AJ, Fallick AE (1989b) Heavy carbon in two-billion-old marbles from Lofoten-Vesteralen, Norway: implications for the Precambrian carbon cycle. Geochim Cosmochim Acta 53(5):1111–1115

Banner JL, Hanson GN (1990) Calculation of simultaneous isotopic and trace element variations during water–rock interaction with applications to carbonate diagenesis. Geochim Cosmochim Acta 54(11):3123–3137

Basta FF, Maurice AE, Fontboté L, Favarger PY (2011) Petrology and geochemistry of the banded iron formation (BIF) of Wadi Karim and Um Anab, Eastern Desert, Egypt: implications for the origin of Neoproterozoic BIF. Precambr Res 187(3):277–292

Bau M (1993) Effects of syn-depositional and postdepositional processes on the rareearth element distribution in Precambrian iron-formations. Eur J Mineral 5:257–267

Bau M, Dulski P, Moller P (1995) Yttrium and holmium in South Pacific seawater: vertical distribution and possible fractionation mechanisms. Chem Erde 55(1):1–15

Bau M, Dulski P (1996) Distribution of yttrium and rare-earth elements in the Penge and Kuruman iron-formations, Transvaal Supergroup, South Africa. Precambr Res 79(1):37–55

Bau M, Dulski P (1999) Comparing yttrium and rare earths in hydrothermal fluids from the Mid-Atlantic Ridge: implications for Y and REE behaviour during near-vent mixing and for the Y/Ho ratio of Proterozoic seawater. Chem Geol 155(1):77–90

Bau M, Höhndorf A, Dulski P, Beukes NJ (1997) Sources of rare-earth elements and iron in Paleoproterozoic iron-formations from the Transvaal Supergroup, South Africa: evidence from neodymium isotopes. J Geol 105(1):121–129

Bekker A, Kaufman AJ, Karhu JA, Beukes NJ, Swart QD, Coetzee LL, Eriksson KA (2001) Chemostratigraphy of the Paleoproterozoic Duitschland Formation, South Africa: implications for coupled climate change and carbon cycling. Am J Sci 301(3):261–285

Bekker A, Kaufman AJ, Karhu JA, Eriksson KA (2005) Evidence for Paleoproterozoic cap carbonates in North America. Precambr Res 137(3):167–206

Bekker A, Slack JF, Planavsky N, Krapež B, Hofmann A, Konhauser KO, Rouxel OJ (2010) Iron formation: the sedimentary product of a complex interplay among mantle, tectonic, oceanic, and biospheric processes. Econ Geol 105(3):467–508

Bolhar R, Van Kranendonk MJ (2007) A non-marine depositional setting for the northern Fortescue Group, Pilbara Craton, inferred from trace element geochemistry of stromatolitic carbonates. Precambr Res 155(3):229–250

Bolhar R, Kamber BS, Moorbath S, Fedo CM, Whitehouse MJ (2004) Characterisation of early Archaean chemical sediments by trace element signatures. Earth Planet Sci Lett 222(1):43–60

Bolhar R, Van Kranendonk MJ, Kamber BS (2005) A trace element study of siderite–jasper banded iron formation in the 3.45 Ga Warrawoona Group, Pilbara Craton—formation from hydrothermal fluids and shallow seawater. Precambr Res 137(1):93–114

Chen YJ, Liu CQ, Chen HY, Zhang ZJ, Li C (2000) Carbon isotope geochemistry of graphite deposits and ore-bearing khondalite series in North China: implications for several geoscientific problems. Acta Petrologica Sinica 16(2):233–244

Cheng YC (1957) Problems on the genesis of the high-grade ore in the pre-Sinian (pre-Cambrian) banded iron ore deposits of the Anshan-type of Liaoning and Shantung provinces. Acta Geol Sin 37(2):153–180

Cheng YQ (1998) Geological research. In: Proceedings of north China platform in early Precambrian, Beijing

Dai YP, Zhang LC, Cl Wang, Liu L, Cui ML, Zhu MT, Xiang P (2012) Genetic type, formation age and tectonic setting of the Waitoushan banded iron formation, Benxi, Liaoning Province. Acta Petrol Sin 28(11):3574–3594

Dai YP, Zhang LC, Zhu MT, Wang CL, Liu L, Xiang P (2014) The composition and genesis of the Mesoarchean Dagushan banded iron formation (BIF) in the Anshan area of the North China Craton. Ore Geol Rev 63:353–373

Danielson A, Möller P, Dulski P (1992) The europium anomalies in banded iron formations and the thermal history of the oceanic crust. Chem Geol 97(1):89–100

Department of Land and Resources of Anhui Province. Geological Survey of Anhui Province (2004) Iron ore resources planning of Huoqiu, Anhui Province. The archives of Department of Land and Resources of Anhui Province

Douville E, Bienvenu P, Charlou JL, Donval JP, Fouquet Y, Appriou P, Gamo T (1999) Yttrium and rare earth elements in fluids from various deep-sea hydrothermal systems. Geochim Cosmochim Acta 63(5):627–643

Gross GA (1980) A classification of iron formations based on depositional environments. Can Mineral 18(2):215–222

Gross GA (1983) Tectonic systems and the deposition of iron-formation. Precambr Res 20(2–4):171–187

Gross GA (1996) Algoma-type previous termiron-formation, Selected British Columbia Mineral Deposits Profiles 2. British Columbia Ministry of Employment and Investment Open File, Ottawa, pp 25–28

Huang H, Zhang LC, Liu XF, Lee HZ, Liu L (2013) Geological and geochemical characteristics of the Lee Laozhuang iron mine in Huoqiu iron deposit: implications for sedimentary environment. Acta Petrol Sin 29(7):2593–2605

Huston DL, Logan GA (2004) Barite, BIFs and bugs: evidence for the evolution of the Earth's early hydrosphere. Earth Planet Sci Lett 220(1):41–55

Isley AE (1995) Hydrothermal plumes and the delivery of iron to banded iron formation. J Geol 103(2):169–185

James HL (1954) Sedimentary facies of iron-formation. Econ Geol 49(3):235–293

James HL (1983) Distribution of banded iron-formation in space and time. Dev Precambr Geol 6:471–490

Jiang SY, Chen CX, Chen YQ, Jiang YH, Dai BZ, Ni P (2004) Geochemistry and genetic model for the giant magnesite

deposits in the eastern Liaoning province China. Acta Petrol Sin 20(4):765–772

Khan RMK, Sharma SD, Patil DJ, Naqvi SM (1996) Trace, rare-earth element, and oxygen isotopic systematics for the genesis of banded iron-formations: evidence from Kushtagi schist belt, Archaean Dharwar Craton, India. Geochim Cosmochim Acta 60(17):3285–3294

Klein C (2005) Some Precambrian banded iron-formations (BIFs) from around the world: their age, geologic setting, mineralogy, metamorphism, geochemistry, and origins. Am Mineral 90(10):1473–1499

Lan TG, Fan HR, Hu FF, Yang KF, Cai YC, Liu YS (2014) Depositional environment and tectonic implications of the Paleoproterozoic BIF in Changyi area, eastern North China Craton: evidence from geochronology and geochemistry of the metamorphic wall-rocks. Ore Geol Rev 61:52–72

Liu L, Yang XY (2015) Temporal, environmental and tectonic significance of the Huoqiu BIF, southeastern North China Craton: geochemical and geochronological constraints. Precambr Res 261:217–233

McLennan SM (1989) Rare earth elements in sedimentary rocks; influence of provenance and sedimentary processes. Rev Mineral Geochem 21(1):169–200

Melezhik VA, Gorokhov IM, Fallick AE, Gjelle S (2001a) Strontium and carbon isotope geochemistry applied to dating of carbonate sedimentation: an example from high-grade rocks of the Norwegian Caledonides. Precambr Res 108(3):267–292

Melezhik VA, Gorokhov IM, Kuznetsov AB, Fallick AE (2001b) Chemostratigraphy of Neoproterozoic carbonates: implications for 'blind dating'. Terra Nova 13(1):1–11

Meschede M (1986) A method of discriminating between different types of mid-ocean ridge basalts and continental tholeiites with the Nb–Zr–Y diagram. Chem Geol 56(3):207–218

Murray RW, Ten Brink MRB, Gerlach D, Russ GP, Jones DL (1991) Rare earth, major, and trace elements in chert from the Franciscan Complex and Monterey Group, California: assessing REE sources to fine-grained marine sediments. Geochim Cosmochim Acta 55(7):1875–1895

Pecoits E, Gingras MK, Barley ME, Kappler A, Posth NR, Konhauser KO (2009) Petrography and geochemistry of the Dales Gorge banded iron formation: paragenetic sequence, source and implications for palaeo-ocean chemistry. Precambr Res 172(1):163–187

Planavsky N, Bekker A, Rouxel OJ, Kamber B, Hofmann A, Knudsen A, Lyons TW (2010) Rare Earth Element and yttrium compositions of Archean and Paleoproterozoic Fe formations revisited: new perspectives on the significance and mechanisms of deposition. Geochim Cosmochim Acta 74(22):6387–6405

Ray JS, Veizer J, Davis WJ (2003) C, O, Sr and Pb isotope systematics of carbonate sequences of the Vindhyan Supergroup, India: age, diagenesis, correlations and implications for global events. Precambr Res 121(1):103–140

Sang BL, Xing FM, Chen YZ (1981) The Precambrian metamorphic iron ore characteristics and prospecting. Anhui Inst Geol Sci 1:10–20

Schidlowski M (1988) A 3,800-million-year isotopic record of life from carbon in sedimentary rocks. Nature 333(6171):313–318

Schidlowski M (1998) Beginnings of terrestrial life: problems of the early record and implications for extraterrestrial scenarios. Paper presented at the SPIE's international symposium on optical science, engineering, and instrumentation

Schidlowski M, Eichmann R, Junge CE (1975) Precambrian sedimentary carbonates: carbon and oxygen isotope geochemistry and implications for the terrestrial oxygen budget. Precambr Res 2(1):1–69

Shen BF, Hui Luo, Li SB, Li JJ, Peng XL, Hu XD, Mao DB, Liang RX (1994) Geology and metallization of Archean greenstone belts in north China platform. Geological Publishing House, Beijing

Shen BF, Zhai AM, Chen WL, Yang CL, Hu XD, Cao XL, Gong XH (2006) The Precambrian mineralization of China. Geological Publishing House, Beijing

Shen QH, Song HX, Zhao ZR (2009) Characteristics of rare earth elements and trace elements in Hanwang Neo-Archaean banded iron formations, Shandong Province. Acta Geosci Sin 30(6):693–699

Stakes DS, O'Neil JR (1982) Mineralogy and stable isotope geochemistry of hydrothermally altered oceanic rocks. Earth Planet Sci Lett 57(2):285–304

Sun YB (2007) Geological characteristics and metallogenic types of the Lilaozhuang iron–magnesite deposit in Huoqiu, Anhui. Mineral Resour Geol 21(5):532–537

Sun SS, McDonough WF (1989) Chemical and isotopic systematics of oceanic basalts: implications for mantle composition and processes. Geol Soc Lond Spec Publ 42(1):313–345

Taylor SR, McLennan SM (1985) The continental crust: its composition and evolution. Blackwell Scientific, USA

Veizer J, Clayton RN, Hinton RW (1992) Geochemistry of Precambrian carbonates: IV. Early Paleoproterozoic (2.25 ± 0.25 Ga) seawater. Geochim Cosmochim Acta 56(3):875–885

Veizer J, Ala D, Azmy K, Bruckschen P, Buhl D, Bruhn F, Carden GAF, Diener A, Ebneth S, Godderis Y (1999) 87Sr/86Sr, δ13C and δ18O evolution of Phanerozoic seawater. Chem Geol 161(1):59–88

Wada H, Suzuki K (1983) Carbon isotopic thermometry calibrated by dolomite–calcite solvus temperatures. Geochim Cosmochim Acta 47(4):697–706

Wan YS, Liu DY, Wang SY, Zhao X, Dong CY, Zhou HY, Yin XY, Yang CX, Gao LZ (2009) Early Precambrian crustal evolution in the Dengfeng area, Henan province (eastern China): constraints from geochemistry and SHRIMP U–Pb zircon dating. Acta Geol Sinica 83(7):982–999

Wang CL, Zhang LC, Lan CY, Dai YP (2014) Rare earth element and yttrium compositions of the Paleoproterozoic Yuanjiacun BIF in the Lüliang area and their implications for the Great Oxidation Event (GOE). Sci China Earth Sci 57(10):2469–2485

Yang XY, Wang BH, Du ZB, Wang QC, Wang YX, Tu ZB, Zhang WL, Sun WD (2012) On the metamorphism of the Huoqiu Group, forming ages and mechanism of BIF and iron deposit in the Huoqiu region, southern margin of North China carton

Yang X, Liu L, Lee IS, Wang B, Du ZB, Wang QC, Wang YX, Sun WD (2014) A review on the Huoqiu banded iron formation (BIF), southeast margin of the North China Craton: genesis of iron deposits and implications for exploration. Ore Geol Rev 63(1):418–443

Zhai MG, Windley BF (1990) The Archaean and early Proterozoic banded iron formations of North China: their characteristics, geotectonic relations, chemistry and implications for crustal growth. Precambr Res 48(3):267–286

Zhai MG, Windley BF, Sills JD (1990) Archaean gneisses, amphibolites and banded iron-formations from the Anshan area of Liaoning Province, NE China: their geochemistry, metamorphism and petrogenesis. Precambr Res 46(3):195–216

Zhang J, Nozaki Y (1996) Rare earth elements and yttrium in seawater: ICP-MS determinations in the East Caroline, Coral Sea, and South Fiji basins of the western South Pacific Ocean. Geochim Cosmochim Acta 60(23):4631–4644

Zhang LC, Zhang XJ, Cui ML, Dai YP, Wang CL, Liu L, Wan YS (2011) Formation age and tectonic environment of BIF iron ore in North China Craton. Acta Mineral Sin 31(2):666–667

Zhang LC, Zhai MG, Wan YS, Guo JH, Dai YP, Wang CL, Li Liu (2012) Study of the Precambrian BIF-iron deposits in the North China Craton: progresses and questions. Acta Petrol Sin 28(11):3431–3445

Zhao ZH (1997) Geochemistry of trace elements. Science Press, Beijing

Zhao GC, Sun M, Wilde SA, Sanzhong L (2005) Late Archean to Paleoproterozoic evolution of the North China Craton: key issues revisited. Precambr Res 136(2):177–202